NASA/TM—1998-207421

Refraction of Sound Emitted Near Solid Boundaries From a Sheared Jet

Loren H. Dill and Ayo A. Oyediran
AYT Corporation, Brook Park, Ohio

Eugene A. Krejsa
Lewis Research Center, Cleveland, Ohio

National Aeronautics and
Space Administration

Lewis Research Center

May 1998

Acknowledgments

The authors express their sincere appreciation to several individuals who made this work possible: to M. Majjigi of GE Aircraft Engines, who defined the problem from an application oriented perspective; to J. Earls, who was instrumental in initiating the project; to J. Shaw for financial support; and to M. E. Goldstein, who helped define the technical problem and provided invaluable technical assistance. The last three individuals above are employees of the NASA Lewis Research Center. This work was supported by NASA contract NAS3-27571.

Available from

NASA Center for Aerospace Information
7121 Standard Drive
Hanover, MD 21076
Price Code: A04

National Technical Information Service
5287 Port Royal Road
Springfield, VA 22100
Price Code: A04

Refraction of Sound Emitted Near Solid Boundaries from a Sheared Jet

L.H. Dill and A.A. Oyediran
AYT Corporation, Brook Park, OH

E. Krejsa
NASA Lewis Research Center, Cleveland, OH

Revised, April 1998

Abstract

A mathematical model is developed to describe the sound emitted from an arbitrary point within a turbulent flow near solid boundaries. A unidirectional, transversely-sheared mean flow is assumed, and the cross-section of the cold jet is of arbitrary shape. The analysis begins with Lilley's formulation of aerodynamic noise and, depending upon the specific model of turbulence used, leads via Fourier analysis to an expression for the spectral density of the intensity of the far-field sound emitted from a unit volume of turbulence. The expressions require solution of a reduced Green's function of Lilley's equation as well as certain moving axis velocity correlations of the turbulence. Integration over the entire flow field is required in order to predict the sound emitted by the complete flow. Calculations are presented for sound emitted from a plug-flow jet exiting a semi-infinite flat duct. Polar plots of the far-field directivity show the dependence upon frequency and source position within the duct. Certain model problems are suggested to investigate the effect of duct termination, duct geometry, and mean flow shear upon the far-field sound.

1 Introduction

There is considerable interest today in developing a new generation of supersonic and subsonic civil transports that are relatively quiet despite their enhanced capabilities. To achieve this noise reduction, improved theoretical models are required to account for effects ignored in previous theories of aerodynamic noise.

In his celebrated analysis of aerodynamically-generated sound, Lighthill [1, 2] rearranged the equations of motion for a compressible fluid to obtain the inhomogeneous wave equation, the basis of classical acoustics for stationary media, for density fluctuations ρ':

$$\nabla^2 \rho' - c_\circ^2 \frac{\partial^2 \rho'}{\partial t^2} = -s(\mathbf{y}, t). \tag{1}$$

Here, $\nabla^2 \equiv \partial^2/\partial y_i^2$ is the Laplacian, c_o the mean speed of sound, t time, and s an acoustic source that Lighthill identified as a convecting quadrupole related to the Reynolds stress tensor. Thus, one of Lighthill's major advances, called *Lighthill's acoustic analogy*, is that the problem of sound generated aerodynamically can be replaced by an equivalent stationary-medium problem involving an acoustic source distribution that incorporates the dynamics of the actual flow. The theory met with considerable early success in predicting major aspects of the radiated sound field of cold jets, and even today the theory and its direct extensions find practical use. Both Goldstein [3] and Lilley [4] provide more recent perspectives on Lighthill's theory.

However, as demonstrated by Lush [5], careful comparison of jet noise data with Lighthill's theory revealed subtle but significant discrepancies, such as the frequency-dependence of the far-field directivity, which the theory was unable to explain. It was gradually recognized that though Lighthill's analogy is exact, there are difficulties in estimating the acoustic source distribution when the radiation is refracted by the flow of the medium.

Inclusion of refractive mean flow effects requires modification of the operator in the governing equation. Lilley [6] derived a nonlinear moving-medium wave equation from the exact transport equations to include these effects. Lilley's equation is considerably more complicated than that used by Lighthill, and this proves to be the equation's major disadvantage. Mani [7, 8], in an effort to retain the simplicity of Lighthill's equation while including convection of the medium, proposed a two- region plug-flow model: (1) an inner region possessing a plug flow surrounded by (2) a stationary region. Goldstein, on the other hand, employed a linearized version of Lilley's equation for unidirectional, transversely sheared mean flows, and showed that in both the low [9, 10] and high [11] frequency limits mean flow shear can significantly influence the directivity in free jets. In these investigations, both Mani and Goldstein modeled the sound source as a convecting multipole.

Lighthill's theory, based upon the free-space Green's function, also failed to account for the diffractive and sound-generating effects of solid surfaces near the turbulent flow, including the effect of duct termination. Goldstein and Rosenbaum [12] accounted for these surface effects in a Lighthill-type formulation. They predicted the far-field directivity in terms of certain correlation scales of the turbulence for a localized, convecting source. Because this theory is based upon Lighthill's formulation, it does not include the refractive effect of mean flow upon the transmission of sound. However, one of its major advantages is that it can associate particular source regions as being relatively noisy or quiet.

On the other hand, Mani [13] and others, including Savkar [14], Munt [15, 16], and Cargill [17]) included mean flow effects in the context of the plug-flow type models for terminating ducts. Mani considered flat ducts while the other investigators focused upon cylindrical ones. Each of these investigations assumed a waveguide, propagating from minus infinity within the duct, served as the source of the sound that radiated to the far-field. Due to their waveguide sources, these models fail to include the convective amplification expected of turbulence-generated sound. Furthermore, these waveguide models fail to provide insight into the relative contributions of certain regions of the flow to the overall directivity.

To investigate the refractive effect of mean shear in the presence of solid surfaces, we here adopt the approach of Goldstein and Rosenbaum but begin with Lilley's equation rather than Lighthill's. We thus obtain a general expression for the spectral density of the far-field intensity due to a unit volume of turbulence within a jet. Then, due to the difficulty in

solving Lilley's equation and to gain insight into this class of problems, we apply the theory to a simplified plug-flow jet problem, and thereby derive explicit expressions to calculate the directivity for a localized source.

The structure of the paper is as follows: In the next section, we derive expressions for the spectral density of the far-field intensity for a localized convecting acoustic source that is located within a turbulent jet. The analysis includes the effect of duct termination and the model applies to unidirectional jets with transversely sheared mean flow of any cross-section. Beginning with a linearized version of Lilley's equation for the acoustic pressure and following a Fourier transformation in time, the transformed pressure is expressed in terms of an integral involving a reduced Green's function of Lilley's equation and a transform of the localized source. Integration by parts is then required to transfer derivatives with respect to source coordinates from the source term to the Green's function. The final expression for the transformed pressure is then given by an integration over the source region of the contracted product of a Reynolds stress tensor and a second-ranked tensor involving gradients of the reduced Green's function and of the mean fluid velocity. An expression for the spectral density of the intensity is then formed and via a set of variable transformations re- expressed in terms of a fourth-order moving axis velocity correlation function. We subsequently focus upon the spectral density of the intensity due to a unit volume of turbulence, and assume that the fourth-order correlations can be adequately represented in terms of second-order correlations to derive a simplified form of the spectral density. This expression is further simplified by assuming the turbulence possesses axisymmetric symmetry. A final expression for the spectral density is obtained upon assuming the turbulence is isotropic.

Section 3 is devoted to the applying the foregoing theory to a plug-flow jet that exits between two parallel plates. A formal solution to the Green's function is obtained using the Wiener-Hopf method of analysis. The analysis is followed through to its completion, and sample plots of the far-field directivity are presented in section 4. Two appendices supplement the Wiener- Hopf analysis.

2 General Theory

Below we consider a jet of arbitrary cross-sectional shape that exits a semi-infinite duct (see Fig. 1) and develop a general expression for the spectral density of the far-field intensity due to a convecting localized acoustic source located within the flow. This general expression for the spectral density is then simplified by application of additional assumptions relative to the nature of the turbulence.

2.1 General Expression for the Spectral Density

Let the total fluid velocity $\mathbf{v}(\mathbf{y}, t)$ at any point $\mathbf{y}$ in the fluid be given by the sum $\mathbf{U}(\mathbf{y}) + \mathbf{u}(\mathbf{y}, t)$. Here, $\mathbf{U}$ represents the mean velocity, $\mathbf{u}$ the fluctuating part with zero mean, and t time. To simplify the analysis, we assume a unidirectional, transversely sheared mean flow, at least in a local sense. Then if $\mathbf{i}_1$ denotes a unit vector in the direction of the jet and $\mathbf{y} = (y_1,\ y_2,\ y_3)$ a Cartesian coordinate system with origin at the end of the duct, the mean flow is of the functional form $\mathbf{i}_1 U(y_2,\ y_3)$. According to Lilley's equation as presented by

Goldstein [3], the pressure variable $\Pi(\mathbf{y},t) = (c_v/c_p)\ln p/p_0$ (with $p = p(\mathbf{y},t)$ the pressure) is then governed by the third-order wave equation

$$\frac{D_o}{Dt}\left(c_0^2\nabla^2\Pi - \frac{D_o^2\Pi}{Dt^2}\right) - 2c_0^2(\nabla U)\cdot\frac{\partial}{\partial y_1}\nabla\Pi = c_0\Gamma/\rho_0, \tag{2}$$

where the acoustic source $\Gamma(\mathbf{y},t)$ is given by the expression

$$\Gamma(\mathbf{y},t) = -\frac{\rho_0}{c_0}\left(\frac{D_o}{Dt}\nabla\cdot\nabla\cdot\mathbf{uu} - 2(\nabla U)\cdot\frac{\partial}{\partial y_1}\nabla\cdot\mathbf{uu}\right). \tag{3}$$

Lilley's equation as given above is derived from the exact equations of motion upon neglect of viscous dissipation and entropy fluctuations and upon linearization about the mean flow. We further assumed that the mean speed of sound c_0 is constant and that the turbulence is incompressible ($\nabla\cdot\mathbf{u}\sim 0$). Appearing above is the heat capacity ratio c_p/c_v, a reference pressure p_0, a reference density ρ_0, and the material derivative $\frac{D_o}{Dt} = \frac{\partial}{\partial t} + U\frac{\partial}{\partial y_1}$. To insure convergence of integrals that will be encountered in the subsequent development, we assume that $\mathbf{uu}$ is identically zero for $|t| > T$, where T represents a large period of time that at the end of the analysis may be taken as infinity.

We next suppose that pressure fluctuations $p - p_0$ are everywhere much less than the ambient pressure p_0. This permits the replacement of Π in Lilley's equation with $(p-p_0)/\rho_0 c_0^2$, where ρ_0 is the mean density. In writing this, we have taken the reference pressure as $p_0 = \rho_0 c_0^2$ with $c_0 = \sqrt{c_p p_0/c_v\rho_0}$, which is valid for an ideal gas whenever fluctuations in entropy may be neglected.

Solid boundaries are assumed to be rigid so that $\mathbf{n}\cdot\mathbf{v}$ must vanish identically. Here, $\mathbf{n}$ represents a unit normal vector directed from the fluid phase into the solid. To derive a boundary condition upon the pressure, we consider the normal component of the momentum equation:

$$\mathbf{n}\cdot\left[\rho(\frac{\partial\mathbf{v}}{\partial t} + \mathbf{v}\cdot\nabla\mathbf{v}) + \nabla p\right] = 0 \tag{4}$$

The first term is identically zero due to the assumption the boundary is rigid. For surfaces located outside the region of turbulent flow, the acoustic approximation applies so that the second term, which involves the square of a perturbation quantity, is negligible. The second term can also be shown to be identically zero for surfaces adjacent to the turbulent flow if the radius of curvature R of the surface in the flow direction is infinite. Otherwise, the second term is given by the potentially large quantity $\pm\rho v^2/R$. To make progress, we assume that R is much greater than, say h, a characteristic distance between boundary surfaces (see Fig. 1). Under these conditions, we may require the normal derivative of the pressure to vanish:

$$\mathbf{n}\cdot\nabla p = \frac{\partial p}{\partial n} = 0 \quad \text{on solid boundaries} \tag{5}$$

In addition to the above requirements, the pressure must satisfy causality and the outgoing radiation condition.

To solve this system of equations, we introduce the Fourier transform $P(\mathbf{y})$ of the pressure with respect to time:

$$P \equiv (p - p_0)^t = \frac{1}{\sqrt{2\pi}} \int_{-\infty}^{\infty} (p - p_0) e^{i\omega t} \, dt \tag{6}$$

Transformation of equation (2) with Π replaced by $(p - p_0)/\rho_0 c_0^2$ gives

$$(-ik + M\frac{\partial}{\partial y_1}) \left[\nabla^2 P - (-ik + M\frac{\partial}{\partial y_1})^2 P \right] - 2(\nabla M) \cdot \frac{\partial}{\partial y_1} \nabla P = \Gamma^t(\mathbf{y}), \tag{7}$$

with $k = \omega/c_0$ the wave number and $M(y_2, y_3) = U/c_0$ the local Mach number of the jet. (The Fourier transform of a quantity with respect to time is denoted by a superscript t.) An expression for the Fourier transform of the source can be obtained from equation (3):

$$\Gamma^t(\mathbf{y}) = -\rho_0 \left[(-ik + M\frac{\partial}{\partial y_1}) \nabla \cdot \nabla \cdot (\mathbf{uu})^t - 2(\nabla M) \cdot \frac{\partial}{\partial y_1} \nabla (\mathbf{uu})^t \right]. \tag{8}$$

The pressure boundary condition on solid surfaces transforms simply to $\frac{\partial P}{\partial n} = 0$. Finally, P is required to satisfy the radiation condition at infinity as well as causality.

A formal solution to P can be expressed in terms of a Green's function G as

$$\begin{aligned} P(\mathbf{x}) &= -\int_{\mathcal{V}} G(\mathbf{x}|\mathbf{y}) \Gamma^t(\mathbf{y}) \, d\mathbf{y} \\ &= \rho_0 \int_{\mathcal{V}} G(\mathbf{x}|\mathbf{y}) \left[(-ik + M\frac{\partial}{\partial y_1}) \nabla \cdot \nabla \cdot (\mathbf{uu})^t - 2(\nabla M) \cdot \frac{\partial}{\partial y_1} \nabla (\mathbf{uu})^t \right] d\mathbf{y}. \end{aligned} \tag{9}$$

Here, $\mathcal{V}$ represents all the volume outside of solid boundaries, but effectively, because the source is localized, the integration need only be performed over that region for which Γ^t is nonzero. The Green's function satisfies the same governing equations and conditions as P, except that a delta function replaces the original source term. Thus, $G(\mathbf{x}|\mathbf{y})$ is governed by the field equation

$$(-ik + M\frac{\partial}{\partial x_1}) \left[\nabla_x^2 G - (-ik + M\frac{\partial}{\partial x_1})^2 G \right] - 2(\nabla_x M) \cdot \frac{\partial}{\partial x_1} \nabla_x G = -\delta(\mathbf{x} - \mathbf{y}), \tag{10}$$

with $\mathbf{n} \cdot \nabla_x G = 0$ on solid boundaries. Finally, we require G to satisfy a radiation condition at infinity and causality. Here, $\nabla_x \equiv \frac{\partial}{\partial \mathbf{x}}$ represents the gradient operator with respect to the observer's coordinates $\mathbf{x}$, and $\mathbf{y}$ now represents the source coordinates.

It is convenient to integrate by parts in equation (9) and thereby transfer all the derivatives with respect to $\mathbf{y}$ to the Green's function. To assist in this process, we define three integrals,

$$I_a = \int_{\mathcal{V}} G \nabla \cdot \nabla \cdot \mathbf{uu} \, d\mathbf{y} \tag{11a}$$

$$I_b = \int_{\mathcal{V}} GM \frac{\partial}{\partial y_1} \nabla \cdot \nabla \cdot \mathbf{uu} \, d\mathbf{y} \tag{11b}$$

$$I_c = \int_{\mathcal{V}} G(\nabla M) \cdot \frac{\partial}{\partial y_1} \nabla \cdot \mathbf{uu} \, d\mathbf{y} \tag{11c}$$

so that P may be expressed as the sum

$$P = \rho_0(-ikI_a + I_b - 2I_c)^t \tag{12}$$

Next, we display certain easily proved vector-dyadic identities that are valid for arbitrary scalar, vector, and symmetric dyadic functions of position $S(\mathbf{y})$, $\mathbf{V}(\mathbf{y})$, and $\mathbf{D}(\mathbf{y})$, respectively:

$$\begin{aligned}
S\nabla\cdot\nabla\cdot\mathbf{D} &= \nabla\cdot\nabla\cdot(S\mathbf{D}) - 2\nabla\cdot(\mathbf{D}\cdot\nabla S) + \mathbf{D}:\nabla\nabla S && \text{(13a)}\\
\nabla\cdot(S\mathbf{V}\mathbf{V}) &= 2S\mathbf{V}\nabla\cdot\mathbf{V} + (\nabla S)\cdot\mathbf{V}\mathbf{V} && \text{(13b)}\\
\mathbf{V}_1 S\cdot\frac{\partial\mathbf{V}_2}{\partial y_1} &= \frac{\partial\mathbf{V}_1 S\cdot\mathbf{V}_2}{\partial y_1} - \frac{\partial\mathbf{V}_1 S}{\partial y_1}\cdot\mathbf{V}_2 && \text{(13c)}\\
\mathbf{V}\cdot\nabla\cdot\mathbf{D} &= \nabla\cdot(\mathbf{D}\cdot\mathbf{V}) - \mathbf{D}:\nabla\mathbf{V}. && \text{(13d)}
\end{aligned}$$

In the third identity, $\mathbf{V}_1$ and $\mathbf{V}_2$ are two distinct vectors.

Now consider integral I_a in conjunction with equation (13a) with S set to G and $\mathbf{D}$ to $\mathbf{uu}$. Integrate the identity over the volume $\mathcal{V}$ and apply Gauss's divergence theorem to the first two integrals. The resulting surface integrals vanish at infinity because both the source and the Green's function vanish in this limit. They also vanish along all solid boundaries due to the condition $\mathbf{n}\cdot\mathbf{v} = \mathbf{n}\cdot\mathbf{u} = 0$. This is easily seen for the second surface integral. That the first integral vanishes along solid boundaries can be seen via the second identity above with S set to G and $\mathbf{V}$ to $\mathbf{u}$. It follows that I_a is given by

$$I_a = \int_{\mathcal{V}} \mathbf{uu} : \nabla\nabla G \; d\mathbf{y}. \tag{14a}$$

In a similar manner, it can be shown using the above identities that I_b and I_c reduce to the volume integrals

$$\begin{aligned}
I_b &= -\int_{\mathcal{V}} \mathbf{uu} : \frac{\partial}{\partial y_1}\nabla\nabla(GM)\; d\mathbf{y} && \text{(14b)}\\
I_c &= \int_{\mathcal{V}} \mathbf{uu} : \frac{\partial}{\partial y_1}\nabla(G\nabla M)\; d\mathbf{y}\\
&\equiv \int_{\mathcal{V}} \mathbf{uu} : \frac{\partial}{\partial y_1}\left[\nabla(G\nabla M)\right]^S\; d\mathbf{y} && \text{(14c)}
\end{aligned}$$

In the latter expression, the superscript S denotes the symmetric portion of the dyadic; e.g. if $\mathbf{a}$ and $\mathbf{b}$ are vectors, the symmetric portion of the dyadic $\mathbf{ab}$ is $(\mathbf{ab} + \mathbf{ba})/2$.

Putting these results together yields the expression for the transform of the acoustic pressure

$$P(\mathbf{x}) = -\rho_0 \int_{\mathcal{V}} (\mathbf{uu})^t : \tilde{\mathbf{G}}(\mathbf{x}|\mathbf{y})\; d\mathbf{y} \tag{15}$$

with the second-ranked tensor $\tilde{\mathbf{G}}$ given by

$$\tilde{\mathbf{G}}(\mathbf{x}|\mathbf{y}) = ik\nabla\nabla G + \frac{\partial}{\partial y_1}\left\{\nabla\nabla(GM) + 2\left[\nabla(G\nabla M)\right]^S\right\}. \tag{16}$$

In this expression, $G \equiv G(\mathbf{x}|\mathbf{y})$ and $M \equiv M(y_2,\ y_3)$.

Because only statistical information is available for the source, we introduce the spectral density of the intensity $I_\omega(\mathbf{x})$. In the far-field at location $\mathbf{x}$, the spectral density is related to P via the expression

$$I_\omega(\mathbf{x}) = \frac{|P|^2}{2Tc_0\rho_0}. \tag{17}$$

As stated previously, the source is presumed to have a duration of $2T$ with T some large period of time. Introduction of the above expression for P then yields

$$I_\omega(\mathbf{x}) = \frac{\rho_0}{2Tc_0}\int_\nu\int_\nu \tilde{\mathbf{G}}(\mathbf{x}|\mathbf{y}') : (\mathbf{u}'\mathbf{u}')^t(\mathbf{u}''\mathbf{u}'')^{t^*} : \tilde{\mathbf{G}}^*(\mathbf{x}|\mathbf{y}'')\ d\mathbf{y}'\ d\mathbf{y}'' \tag{18}$$

for the spectral density. The asterisk denotes the complex conjugate.

We now use the fact that the Fourier transform of a convolution is proportional to the product of the Fourier transforms of the two components, and that, provided $f(t)$ is real, the Fourier transform of $f(-t)$ is the complex conjugate of the Fourier transform of $f(t)$. It is then easily shown that

$$(\mathbf{u}'\mathbf{u}')^t(\mathbf{u}''\mathbf{u}'')^{t^*} = \frac{T}{\pi}\int_{-\infty}^{\infty} \overline{\mathbf{u}'\mathbf{u}'\mathbf{u}''\mathbf{u}''}e^{-i\omega\tau}\ d\tau \tag{19}$$

where the fourth-order, two-point, two-time velocity correlation tensor is given by

$$\overline{\mathbf{u}'\mathbf{u}'\mathbf{u}''\mathbf{u}''} \ = \ \frac{1}{2T}\int_{-T}^{T} \mathbf{u}(y',\ t)\mathbf{u}(y',\ t)\mathbf{u}(y'',\ t+\tau)\mathbf{u}(y'',t+\tau)\ dt \tag{20}$$

Here, single primes on velocity $\mathbf{u}$ denote position and time $(\mathbf{y}',\ t)$ and double primes position and time $(\mathbf{y}'',\ t+\tau)$.

We now decompose this correlation tensor as

$$\overline{\mathbf{u}'\mathbf{u}'\mathbf{u}''\mathbf{u}''} \ = \ \mathcal{R}_4(\mathbf{y}',\ \mathbf{y}''-\mathbf{y}',\ \tau) + \overline{\mathbf{u}'\mathbf{u}'}\ \overline{\mathbf{u}''\mathbf{u}''}, \tag{21}$$

with $\mathcal{R}_4$ the fourth-order velocity correlation tensor

$$\mathcal{R}_4(\mathbf{y}',\ \mathbf{y}''-\mathbf{y}',\ \tau) \ = \ \overline{\mathbf{u}'\mathbf{u}'\mathbf{u}''\mathbf{u}''} - \overline{\mathbf{u}'\mathbf{u}'}\ \overline{\mathbf{u}''\mathbf{u}''}. \tag{22}$$

Note that due to the assumption that the process is stationary, the correlation tensor $\overline{\mathbf{u}'\mathbf{u}'}\ \overline{\mathbf{u}''\mathbf{u}''}$ is independent of τ. Thus, integration of this term over τ in equation (19) will lead to the delta function $\delta(\omega)$. Consequently, this term is possibly nonzero only at zero frequency, $\omega = 0$. An argument can be made that the contribution of this term to the spectral density is identically zero (see, e.g., Goldstein and Rosenbaum [12]) even for $\omega = 0$, a frequency which is of no physical interest. In any case, we now ignore this contribution and write the spectral density in terms of $\mathcal{R}_4(\mathbf{y}',\ \mathbf{y}''-\mathbf{y}',\ \tau)$ as

$$I_\omega(\mathbf{x}) = \frac{\rho_0}{2\pi c_0}\int_{-\infty}^{\infty}\int_\nu\int_\nu \tilde{\mathbf{G}}(\mathbf{x}|\mathbf{y}') : \mathcal{R}_4(\mathbf{y}',\ \mathbf{y}''-\mathbf{y}',\ \tau) : \tilde{\mathbf{G}}^*(\mathbf{x}|\mathbf{y}'')e^{-i\omega\tau}\ d\mathbf{y}'\ d\mathbf{y}''\ d\tau. \tag{23}$$

The above expression can be simplified a great deal. We first note the assumption that the turbulence is stationary in time leads to a useful symmetry property of $\mathcal{R}_4(\mathbf{y}',\ \mathbf{y}''-\mathbf{y}',\ \tau)$.

Specifically, in equation (22) interchange primed and double primed quantities and replace τ by $-\tau$. Due to stationarity, the resulting integral corresponding to equation (20) must be independent of a translation in time. Upon replacing the variable t with $t+\tau$, we obtain the result in Cartesian tensor notation

$$\begin{aligned}\mathcal{R}_4(\mathbf{y}',\ \mathbf{y}''-\mathbf{y}',\ \tau) &\equiv \mathcal{R}_{ijkl}(\mathbf{y}',\ \boldsymbol{\eta},\ \tau) = \mathcal{R}_{klij}(\mathbf{y}'',\ \boldsymbol{\eta}^{(1)},\ -\tau) \\ &= \frac{1}{2}\mathcal{R}_{ijkl}(\mathbf{y}',\ \boldsymbol{\eta},\ \tau) + \frac{1}{2}\mathcal{R}_{klij}(\mathbf{y}'',\ \boldsymbol{\eta}^{(1)},\ -\tau), \end{aligned} \tag{24}$$

with $\boldsymbol{\eta}= \mathbf{y}''-\mathbf{y}' = -\boldsymbol{\eta}^{(1)}$ separation vectors. This expression is then introduced into the above expression for the spectral density, and it is easily shown that the second term is the complex conjugate of the first, thereby leading to the expression

$$I_\omega(\mathbf{x}) = \frac{\rho_0}{2\pi c_0}\Re\int_{-\infty}^{\infty}\int_{\mathcal{V}}\int_{\mathcal{V}} \tilde{\mathbf{G}}(\mathbf{x}|\mathbf{y}') : \mathcal{R}_4(\mathbf{y}',\ \boldsymbol{\eta},\ \tau) : \tilde{\mathbf{G}}^*(\mathbf{x}|\mathbf{y}'+\boldsymbol{\eta}\ )\mathrm{e}^{-\mathrm{i}\omega\tau}\ d\mathbf{y}'\ d\boldsymbol{\eta}\ d\tau, \tag{25}$$

where $\Re$ denotes the real operator.

It is helpful to introduce two further changes in the variables of integration. We introduce a new vector $\mathbf{y}$,

$$\mathbf{y} \equiv \left(y'_1,\ \frac{y'_2+y''_2}{2},\ \frac{y'_3+y''_3}{2}\right), \tag{26}$$

which together with $\boldsymbol{\eta}$ replaces $\mathbf{y}'$ in the above integrals. With respect to the original vectors $\mathbf{y}'$ and $\mathbf{y}''$, $\mathbf{y}$ represents an average of the transverse locations but the same location as $\mathbf{y}'$ with respect to the component in the direction of flow.

A further change in the variables of integration takes into account the convection of the source: replace $(\boldsymbol{\eta},\ \tau)$ with $(\boldsymbol{\xi},\ \tilde{\tau})$ via the definitions

$$\boldsymbol{\xi} = \boldsymbol{\eta} - \mathrm{i}_1 U_c\tau, \tag{27a}$$

$$\tilde{\tau} = \tau. \tag{27b}$$

After this change in variables, replace the dummy variable of integration $\tilde{\tau}$ with τ and so obtain the expression for the spectral density

$$\begin{aligned} I_\omega(\mathbf{x}) = \frac{\rho_0}{2\pi c_0}\Re\int_{-\infty}^{\infty}\int_{\mathcal{V}}\int_{\mathcal{V}} &\tilde{\mathbf{G}}(\mathbf{x}|\mathbf{y}+(\mathrm{i}_1\xi_1-\boldsymbol{\xi})/2) : \\ &\tilde{\mathcal{R}}_4(\mathbf{y},\ \boldsymbol{\xi},\ \tau) : \tilde{\mathbf{G}}^*(\mathbf{x}|\mathbf{y}+(\mathrm{i}_1\xi_1+\boldsymbol{\xi})/2+\mathrm{i}_1 U_c\tau)\mathrm{e}^{-\mathrm{i}\omega\tau}\ d\mathbf{y}\ d\boldsymbol{\xi}\ d\tau, \end{aligned} \tag{28}$$

where

$$\tilde{\mathcal{R}}_4(\mathbf{y},\ \boldsymbol{\xi},\ \tau) = \mathcal{R}_4(\mathbf{y}+(\mathrm{i}_1\xi_1-\boldsymbol{\xi})/2,\ \boldsymbol{\xi}+\mathrm{i}_1 U_c\tau,\ \tau). \tag{29}$$

is the moving axis correlation function. In the above expression for the spectral density, $\mathcal{V}$ represents the same physical volume (but in the new coordinates) as in the original variables.

Now, according to the argument of Goldstein and Rosenbaum [12], the typical correlation length l of the turbulence in the moving frame is small compared to a typical dimension h of the duct boundary (see Fig. 1); i.e., $l \ll h$. On the other hand, the length scales that

appear within the Green's function (see equation (10)) are the wavelength k^{-1}, h, and $h^{(1)}$, where $h^{(1)}$ is a characteristic distance over which gradients of the mean velocity change. If the correlation length is also much less than the wavelength and $h^{(1)}$, the following argument can be made to simplify the above expression for the spectral density of the intensity: First, by definition of the correlation length, if $|\boldsymbol{\xi}| > l$, then $\tilde{\mathcal{R}}_4(\mathbf{y}, \boldsymbol{\xi}, \tau) \sim 0$. But, because l is much smaller than any length scale that appears within G, the Green's function is nearly constant for $0 \leq |\boldsymbol{\xi}| \leq l$. Consequently, under these conditions, $\boldsymbol{\xi}$ in the arguments of the Green's functions may be set equal to zero in the above expression for the spectral density. This permits us to obtain

$$I_\omega(\mathbf{x}) = \frac{\rho_0}{2\pi c_0} \Re \int_{-\infty}^{\infty} \int_{\nu} \tilde{\mathbf{G}}(\mathbf{x}|\mathbf{y}) : \left[\int \tilde{\mathcal{R}}_4(\mathbf{y}, \boldsymbol{\xi}, \tau)\, d\boldsymbol{\xi} \right] : \tilde{\mathbf{G}}^*(\mathbf{x}|\mathbf{y} + \mathbf{i}_1 U_c \tau) e^{-i\omega\tau}\, d\mathbf{y}\, d\tau, \quad (30)$$

where the omission of integral limits denotes the integration is to be performed over all space.

We also expect the above step to be valid for thin shear layers. If a shear layer of thickness $h^{(1)}$ is much smaller than the correlation length ($h^{(1)} \ll l$) and the source is located outside of and not too close to the shear layer, we expect the Green's function in the far-field to be relatively independent of both of these length scales. In any case, upon calculation of the Green's function and knowledge of the length l, the validity of this step can be evaluated.

For design purposes, interest usually centers not in the prediction of the total far-field sound, but rather in ascertaining the regions of the flow that produce an inordinate amount of sound in the far-field. For this purpose, we let $I_\omega(\mathbf{x}|\mathbf{y})$ denote the spectral density of the intensity at $\mathbf{x}$ due to a source at location $\mathbf{y}$:

$$I_\omega(\mathbf{x}) = \int_{\nu} I_\omega(\mathbf{x}|\mathbf{y})\, d\mathbf{y}. \quad (31)$$

From the above relations, we see that $I_\omega(\mathbf{x}|\mathbf{y})$ is given by

$$I_\omega(\mathbf{x}|\mathbf{y}) = \frac{\rho_0}{2\pi c_0} \Re \left\{ \tilde{\mathbf{G}}(\mathbf{x}|\mathbf{y}) : \int_{-\infty}^{\infty} \left[\int \tilde{\mathcal{R}}_4(\mathbf{y}, \boldsymbol{\xi}, \tau)\, d\boldsymbol{\xi} \right] : \tilde{\mathbf{G}}^*(\mathbf{x}|\mathbf{y} + \mathbf{i}_1 U_c \tau) e^{-i\omega\tau}\, d\tau \right\}. \quad (32)$$

To obtain the total spectral density in the far-field, the above equation would need to be integrated over all the noise-producing regions.

Further simplification of the above equation is not possible without making additional assumptions concerning the nature of the turbulence.

2.2 Reduction in Order of Turbulence Correlations

Goldstein and Rosenbaum [12] suggest representing fourth-order velocity correlations in terms of second-order correlations, not only for $\tau = 0$ as Batchelor had done, but for $\tau \neq 0$. Batchelor's original suggestion (and we now resort to Cartesian tensor notation),

$$\overline{u_i' u_j' u_k'' u_l''} = \overline{u_i' u_j'}\ \overline{u_k'' u_l''} + \overline{u_i' u_k'}\ \overline{u_j'' u_l''} + \overline{u_i' u_l'}\ \overline{u_j'' u_k''} \quad \text{at } \tau = 0, \quad (33)$$

is based upon the assumption that the part of the joint probability of the velocity (with zero time delay) associated with the energy-bearing eddies is approximately normal. Goldstein and Rosenbaum extend this reasoning by saying that if the velocity correlations are separated

in both space and time, the central limit theorem suggests the joint probability distribution would be even closer to a normal distribution. In light of this, equations (22, 29) indicate the fourth-order correlation $\tilde{\mathcal{R}}_4(\mathbf{y},\ \boldsymbol{\xi},\ \tau) \equiv \tilde{\mathcal{R}}_{ijkl}(\mathbf{y},\ \boldsymbol{\xi},\ \tau)$ can be written as

$$\tilde{\mathcal{R}}_{ijkl}(\mathbf{y},\ \boldsymbol{\xi},\ \tau) = \tilde{\mathcal{R}}_{ik}\tilde{\mathcal{R}}_{jl} + \tilde{\mathcal{R}}_{il}\tilde{\mathcal{R}}_{jk}, \tag{34}$$

where the second-order velocity correlation is defined by

$$\tilde{\mathcal{R}}_{ij}(\mathbf{y},\ \boldsymbol{\xi},\ \tau) \equiv \overline{u_i' u_j''} \tag{35}$$

When this result is introduced into equation (32) and the symmetric property of $\tilde{\mathbf{G}}$ is considered, the spectral density may be written as

$$I_\omega(\mathbf{x}|\mathbf{y}) = \frac{\rho_0}{\pi c_0}\Re\left[\tilde{G}_{ij}\int_{-\infty}^{\infty} \mathrm{e}^{-\mathrm{i}\omega\tau}\tilde{G}_{kl}^T \int \tilde{\mathcal{R}}_{ik}\tilde{\mathcal{R}}_{jl},\ d\boldsymbol{\xi}\ d\tau\right]. \tag{36}$$

Here, we have suppressed the $\mathbf{x}$ and $\mathbf{y}$ dependence of $\tilde{G}_{ij}(\mathbf{x}|\mathbf{y})$ and introduced the abbreviated notation

$$\tilde{G}_{ij}^T \equiv \tilde{G}_{ij}^*(\mathbf{x}|\mathbf{y} + \mathbf{i}_1 U_c \tau) \tag{37}$$

2.3 Axisymmetric Turbulence

Turbulence measurements (see [18]) indicate that $\tilde{\mathcal{R}}_{ij}$ is approximately an even function of τ, at least for jet mixing regions. Furthermore, under the assumption of locally axisymmetric turbulence, Goldstein and Rosenbaum [19] contend the correlation tensor may be represented by

$$\tilde{\mathcal{R}}_{ij}(\mathbf{y},\ \boldsymbol{\xi},\ \tau) = A\xi_i\xi_j + B\delta_{ij} + C\delta_{1i}\delta_{1j} + D(\delta_{1i}\xi_j + \delta_{1j}\xi_i), \tag{38}$$

where A, B, and C are functions of $\mathbf{y}$, τ, and $\xi = |\boldsymbol{\xi}|$ and are even functions of ξ_1. The coefficient D is also a function of $\mathbf{y}$, τ, and $\xi = |\boldsymbol{\xi}|$, but is odd with respect to ξ_1. Goldstein and Rosenbaum [12] show that this assumption leads to the spectral density expression

$$I_\omega(\mathbf{x}|\mathbf{y}) = \frac{\rho_0}{\pi c_0}\Re\left\{\int_{-\infty}^{\infty} \mathrm{e}^{-\mathrm{i}\omega\tau}\left[\tilde{G}_{ii}\tilde{G}_{jj}^T S - (\tilde{G}_{22}\tilde{G}_{33}^T + \tilde{G}_{33}\tilde{G}_{22}^T)(Q_{23} - Q_{22}) + \tilde{G}_{ij}\tilde{G}_{ij}^T Q_{ij}\right]\ d\tau\right\}. \tag{39}$$

following extensive algebraic manipulations. (This expression differs slightly from that obtained by Goldstein and Rosenbaum in that we are unable to apply a reciprocity relationship that is valid for a Green's function of the Helmholtz equation.) Here, $Q_{ij} = Q_{ji}$ and

$$Q_{11} = \int(\tilde{\mathcal{R}}_{11}^2 - \tilde{\mathcal{R}}_{12}^2)\ d\boldsymbol{\xi} \tag{40a}$$

$$Q_{12} = Q_{13} = \int(\tilde{\mathcal{R}}_{12}^2 + \tilde{\mathcal{R}}_{11}\tilde{\mathcal{R}}_{22})\ d\boldsymbol{\xi} \tag{40b}$$

$$Q_{22} = Q_{33} = \int(\tilde{\mathcal{R}}_{22}^2 - \tilde{\mathcal{R}}_{12}^2)\ d\boldsymbol{\xi} \tag{40c}$$

$$Q_{23} = \int(\tilde{\mathcal{R}}_{22}^2 - \tilde{\mathcal{R}}_{23}^2)\ d\boldsymbol{\xi} \tag{40d}$$

$$S = \int \tilde{\mathcal{R}}_{12}^2\ d\boldsymbol{\xi} \tag{40e}$$

These five integrals depend only upon four correlations: $\tilde{\mathcal{R}}_{11}$, $\tilde{\mathcal{R}}_{22}$, $\tilde{\mathcal{R}}_{12}$, and $\tilde{\mathcal{R}}_{23}$.

2.4 Isotropic Turbulence

Considerable simplification of the spectral density expression can be obtain upon assuming the turbulence is locally isotropic in the moving reference frame. Then coefficients C and D in equation (38) are identically zero, and the expression for the correlation tensor reduces to

$$\tilde{\mathcal{R}}_{ij}(\mathbf{y},\ \boldsymbol{\xi},\ \tau) = A\xi_i\xi_j + B\delta_{ij}, \tag{41}$$

where A and B are functions only of ξ and τ. In this case, define a correlation scale $L(\mathbf{y},\ \tau)$,

$$L(\mathbf{y},\ \tau) = \frac{1}{\left(\overline{u^2}\right)^2} \int \tilde{R}_{11}^2\ d\boldsymbol{\xi}, \tag{42}$$

where $\sqrt{\overline{u^2}}$ is the rms of the turbulent velocity at $\mathbf{y}$. Then Goldstein and Rosenbaum [12] show that

$$Q_{ij} = \frac{7}{8}\left(\overline{u^2}\right)^2 L \tag{43}$$

for $i,\ j = 1,\ 2,\ 3$, and

$$S = \frac{1}{8}\left(\overline{u^2}\right)^2 L. \tag{44}$$

Clearly, it follows that the spectral density of the intensity may be written as

$$I_\omega(\mathbf{x}|\mathbf{y}) = \frac{7\rho_0\left(\overline{u^2}\right)^2}{8\pi c_0} \Re\left[\int_{-\infty}^{\infty} \mathrm{e}^{-\mathrm{i}\omega\tau}\left(\frac{1}{7}\tilde{G}_{ii}\tilde{G}^T_{jj} + \tilde{G}_{ij}\tilde{G}^T_{ij}\right) L\ d\tau\right]. \tag{45}$$

It should be recalled that $\tilde{G}_{ij}$ is a constant with respect to τ in this expression.

Determination of the far-field directivity due to a source at $\mathbf{y}$ has thus been reduced to finding the Green's solution G of equation (10) in the far-field and then forming $\tilde{\mathbf{G}}$, as defined in equation (16). Then, together with appropriate knowledge of the turbulence, the spectral density of the intensity at $\mathbf{x}$ due to a source at $\mathbf{y}$ may be found from equations (36), (39), or (45) according to whether the turbulence in the moving frame has no special symmetry properties, is axisymmetric, or is isotropic, respectively.

3 Application to a Plug-Flow Jet Exiting a Flat Duct

As mentioned previously, the Lilley equation that governs the Green's function that appears in the above theory has few known exact solutions, and so it is expected that certain approximations will be required to make progress. In this section, we apply the above theory to a simple model problem.

3.1 Formulation

One of the simplest relevant problems is that of a 2-D, plug-flow subsonic jet of thickness $2b$ exiting a flat duct into a resting medium (see Fig. 2). In this model, vortex sheets of effectively zero thickness separate the jet outside the duct from the two fluid layers at rest. The equation (10) that governs G can then be replaced by two simpler equations in which M, the local jet Mach number, is constant. Current boundary conditions on the Green's function must be supplemented with conditions across the vortex sheets [3]; specifically, pressure and particle displacement must be continuous across the sheets. Furthermore, we must specify that the sheets are attached to the end of the duct walls as well as their departing slopes. Application of these latter conditions require that we revert to a kinematical description of the problem; i.e., we must recast the problem in terms of a velocity potential .

The assumption of a plug flow within the jet also permits simplification of the expression for $\tilde{\mathbf{G}}$ in equation (16). Specifically, we obtain

$$\tilde{\mathbf{G}} = \nabla\nabla\mathcal{L}G, \tag{46}$$

where $\mathcal{L} = \mathrm{i}k + M\frac{\partial}{\partial y_1}$. Application of this operator to the equation governing G together with the relation $\mathcal{L}\delta(\mathbf{x}-\mathbf{y}) \equiv (\mathrm{i}k - M\frac{\partial}{\partial x_1})\delta(\mathbf{x}-\mathbf{y})$ yields

$$\begin{aligned} (\nabla_x^2 + k^2)\,\mathcal{L}G &= 0 && \text{for } |x_2| > b \\ \nabla_x^2\mathcal{L}G + k^2\left(1 + \tfrac{\mathrm{i}M}{k}\tfrac{\partial}{\partial x_1}\right)^2\mathcal{L}G &= \delta(\mathbf{x}-\mathbf{y}) && \text{for } |x_2| < b, \end{aligned} \tag{47}$$

following integration.

We now regard $\mathcal{L}G$ as the Fourier transform of "pressure" in time, and seek to solve the corresponding problem for the velocity potential $\phi(x_1,\ x_2)$. It is evident that ϕ satisfies (compare with Mani [13])

$$\begin{aligned} (\nabla_x^2 + k^2)\,\phi &= 0 && \text{for } |x_2| > b \\ \nabla_x^2\phi + k^2\left(1 + \tfrac{\mathrm{i}M}{k}\tfrac{\partial}{\partial x_1}\right)^2\phi &= \mathcal{S}(\mathbf{x}|\mathbf{y}) && \text{for } |x_2| < b \end{aligned} \tag{48}$$

in the bulk fluids. Due to the relation between velocity potential and pressure within the jet, the above source term $\mathcal{S}$ must satisfy

$$\mathrm{i}kc_0\rho_0[1 + (\mathrm{i}M/k)\frac{\partial}{\partial x_1}]\mathcal{S}(\mathbf{x}|\mathbf{y}) = \delta(\mathbf{x}-\mathbf{y}). \tag{49}$$

Along the rigid walls of the duct, ϕ satisfies the zero gradient condition

$$\partial\phi/\partial x_2 = 0 \text{ for } x_1 < 0 \text{ and } x_2 = \pm b. \tag{50}$$

Continuity of pressure along the vortex sheets requires

$$\phi(x_1, b+) = [1 + (\mathrm{i}M/k)\tfrac{\partial}{\partial x_1}]\phi(x_1, b-) \tag{51a}$$

$$[1 + (\mathrm{i}M/k)\tfrac{\partial}{\partial x_1}]\phi(x_1, -b+) = \phi(x_1, -b-) \tag{51b}$$

for $x_1 > 0$. (The plus or minus signs following the symbol b denote the addition or subtraction, respectively, of an infinitesimal positive quantity such that evaluation is taken on

the appropriate side of the duct walls or vortex sheet.) Furthermore, the displacements $\eta(x_1, \pm b)$ of the vortex layers from the respective mean positions at $x_2 = \pm b$ are related to the velocity potentials via

$$\eta(x_1, \pm b) = \tfrac{\mathrm{i}}{kc_0} \tfrac{\partial \phi(x_1, x_2)}{\partial x_2}|_{x_2 = \pm b \pm} \tag{52a}$$

$$[1 + (\mathrm{i}M/k)\tfrac{\partial}{\partial x_1}]\eta(x_1, \pm b) = \tfrac{\mathrm{i}}{kc_0} \tfrac{\partial \phi(x_1, x_2)}{\partial x_2}|_{x_2 = \pm b \mp} \tag{52b}$$

for $x_1 > 0$. In addition to the above requirements, we require the sheets to be attached to the ends of the duct walls and to depart with zero slope (Kutta condition). Furthermore, we seek a solution that satisfies both causality and the radiation condition; the Helmholtz instability, however, precludes full satisfaction of the latter condition.

3.2 Formal Far-Field Solution via the Wiener-Hopf Method

The above equations for the velocity potential constitute a classical Wiener-Hopf problem due to certain boundary conditions prescribed on the semi-infinite duct ($x_1 < 0$) with other conditions prescribed on the semi-infinite vortex layer ($x_1 > 0$).

Noble [20] describes in detail how such problems are solved. The basic idea is to assume the wavenumber k has a small imaginary component, which here is taken as positive. Fourier transformation of the governing field equations with respect to the spatial coordinate x_1 leads to a set of differential equations that can be solved with constants of integration to be determined from proper application of the boundary conditions. Fourier transformation of the boundary conditions lead to functions in the complex α-space that are analytic in either the "plus" or "minus" regions; these are denoted by subscripts $+$ and $-$, respectively. Here, α is the Fourier variable associated with x_1. The plus and minus regions are assumed to possess a small region of overlap due to the small imaginary component of k. The goal of the Wiener-Hopf method is to eliminate unknowns in such a way so as to obtain functions that are analytic in the minus and plus regions on opposite sides of an equation. Then, because of the common domain of analyticity, the one expression must be the analytic continuation of the other. The two sides of the equation then represent an entire function in the complex α-plane. If the solution is unique, it can be shown that the entire function is identically zero for all α. Integration constants can then be determined, and the solution in the Fourier transform space is formally determined. Inversion then leads to the desired result.

We define the Fourier transform of ϕ as $\Phi = \Phi_+ + \Phi_-$ with functions Φ_+ and Φ_- analytic in the plus and minus regions, respectively. These functions are related by the equation

$$\Phi_\pm(\alpha, x_2, k|\mathbf{y}) = \int_{-\infty}^{\infty} H(\pm x_1)\phi(x_1,\ x_2;\ k|\mathbf{y})\mathrm{e}^{\mathrm{i}k\alpha x_1}\ dx_1. \tag{53}$$

Here, $H(x)$ represents the unit Heavyside step function. In the subsequent Wiener-Hopf analysis, we usually suppress the dependence of Φ and similar functions upon k, and $\mathbf{y}$, and further adopt the notation of Noble; i.e., we simply write $\Phi_+(\alpha, x_2) \equiv \Phi_+(\alpha) \equiv \Phi_+(x_2) \equiv \Phi_+$ according to whichever form is convenient provided there is no risk of confusion.

Fourier transformation of equation (47) then leads to the set of equations

$$\Phi'' - k^2\gamma^2\Phi = 0 \text{ for } |x_2| > b \tag{54}$$

$$\Phi'' - k^2\varpi^2\Phi = \frac{\delta(x_2 - y_2)\exp(\mathrm{i}k\alpha y_1)}{\mathrm{i}kc_0\rho_0(1 + M\alpha)} \text{ for } |x_2| < b \tag{55}$$

with primes denoting derivatives with respect to x_2. Scalars γ and ϖ are defined by the relations

$$\begin{aligned} \gamma(\alpha) &= (\alpha^2-1)^{1/2} \\ &\equiv (\alpha-1)^{1/2}(\alpha+1)^{1/2} \qquad (56) \\ \varpi(\alpha) &= [\alpha^2-(1+M\alpha)^2)]^{1/2} \\ &\equiv (1-M^2)^{1/2}(\alpha-\alpha_L)^{1/2}(\alpha-\alpha_U)^{1/2}, \qquad (57) \end{aligned}$$

where $\alpha_L = -1/(1+M)$ and $\alpha_U = 1/(1-M)$. We further define the branch cuts for γ and for ϖ as ± 1 to $\pm\infty$ and $\pm(1\mp M)^{-1}$ to $\pm\infty$, respectively, and require both functions to be positive for $\alpha \to \infty - \mathrm{i}0$. The common strip S and the plus and minus analytical regions in the complex α-plane, $R_{(+)}$ and $R_{(-)}$, respectively, are displayed in Fig. 3. If we assume that $k = |k|\exp(\mathrm{i}\delta)$ and no other singularities are present in the region, the strip may be described as the region between the two lines in the complex α plane that pass through the points $\alpha = \alpha_L$ and $\alpha = 1$ with slope $-\tan\delta$. If $\delta < \pi/2$ as displayed in the figure, the plus region is to the right and above the line passing through $\alpha = \alpha_L$. Similarly, the minus region is to the left and below the line passing through $\alpha = 1$. It can be demonstrated that $\Re(k\gamma)$ and $\Re(k\varpi)$ are positive throughout S. If other singularities are present within the described strip, the thickness of the strip can be reduced as necessary to exclude these singularities as long as there is a common region of overlap.

It is convenient to decompose Φ as $\Phi = \Psi + V$, where $\Psi(x_2)$ satisfies the homogeneous portion of equations (54, 55). On the other hand, the function $V(x_2)$ represents a free space Green's function within the jet in that it satisfies the source term in equation (55), but no specified conditions on the duct or vortex sheets. In particular, we take V as

$$V(x_2) = \begin{cases} 0 & \text{for } x_2 > b \\ \frac{\mathrm{i}\exp(\mathrm{i}k\alpha y_1 - k\varpi|x_2-y_2|)}{2k^2\varpi c_0\rho_0(1+M\alpha)} & \text{for } x_2 \le b \end{cases} \qquad (58)$$

Application of the radiation condition to Ψ yields the result

$$\Psi(x_2) = \begin{cases} A\mathrm{e}^{-k\gamma x_2} & \text{for } x_2 > b \\ B\mathrm{e}^{-k\varpi x_2} + C\mathrm{e}^{k\varpi x_2} & \text{for } |x_2| < b \\ D\mathrm{e}^{k\gamma x_2} & \text{for } x_2 < -b \end{cases}, \qquad (59)$$

where integration constants A, B, C, and D must be determined from application of the boundary conditions along the duct and vortex sheets. (There should be no risk of confusing these four constants of integration with identical symbols that appear in connection with the turbulence correlation tensor in, e.g., equation (38).)

We now adopt the method advocated by Noble on page 125 of his book to obtain the pair of Wiener-Hopf equations associated with the current problem. Let $S^{(o)}$ and $D^{(o)}$ be defined as the sum and difference of Ψ evaluated just outside the duct and vortex layers:

$$S^{(o)} = \Psi(+b+) + \Psi(-b-) \qquad (60a)$$

$$D^{(o)} = \Psi(+b+) - \Psi(-b-) \qquad (60b)$$

The notation $S^{(i)}$ and $D^{(i)}$ is similarly used to denote the sum and difference of Ψ evaluated just inside the duct and vortex layers, and $S^{(V)}$ and $D^{(V)}$ the sum and difference of V

evaluated exactly at $x_2 = b$ and $x_2 = -b$. Primes, e.g., $S^{(o)'}$, denote the sum or difference of the function derivatives with respect to x_2 evaluated at $x_2 = \pm b$. These sums and differences may be decomposed into plus and minus functions, e.g., $S^{(o)} = S_+^{(o)} + S_-^{(o)}$. Lastly, we note that because V is given in (58), the quantities $S_\pm^{(V)}$ and $D_\pm^{(V)}$ and the related primed quantities are known in principle at this stage of the analysis. As is seen later, the decomposition of a known function into plus and minus functions can be accomplished via an integration in the complex α-plane.

It is easy to demonstrate from these definitions and equation (59) the following identities for the 'outer' sums and differences:

$$S^{(o)} = (A + D)\mathrm{e}^{-kb\gamma} \tag{61a}$$

$$D^{(o)} = (A - D)\mathrm{e}^{-kb\gamma} \tag{61b}$$

$$S^{(o)'} = S_+^{(o)'} = -k\gamma(A - D)\mathrm{e}^{-kb\gamma} \tag{61c}$$

$$D^{(o)'} = D_+^{(o)'} = -k\gamma(A + D)\mathrm{e}^{-kb\gamma} \tag{61d}$$

We obtained the extra relation in the latter two equations from the assumption the duct is rigid, i.e., equation (50) requires $S_-^{(o)'} = D_-^{(o)'} = 0$. From the above set of equations, it clearly follows that elimination of A and D leads to

$$S_+^{(o)'} = -k\gamma D^{(o)} \tag{62a}$$

$$D_+^{(o)'} = -k\gamma S^{(o)}. \tag{62b}$$

A similar procedure for the inner fields yields

$$S^{(i)} = 2(C + B)\cosh kb\varpi \tag{63a}$$

$$D^{(i)} = 2(C - B)\sinh kb\varpi \tag{63b}$$

$$S^{(i)'} = 2k\varpi(C - B)\cosh kb\varpi \tag{63c}$$

$$D^{(i)'} = 2k\varpi(C + B)\sinh kb\varpi, \tag{63d}$$

and elimination of B and C gives

$$S^{(i)'} = k\varpi D^{(i)}\coth kb\varpi \tag{64a}$$

$$D^{(i)'} = k\varpi S^{(i)}\tanh kb\varpi. \tag{64b}$$

The above conditions derive largely from the differential equations and application of the radiation condition. We now consider the remaining requirements of conditions imposed along the duct and vortex sheets. The rigid boundaries on the inside of the ducts require

$$S_-^{(i)'} + S_-^{(V)'} = D_-^{(i)'} + D_-^{(V)'} = 0. \tag{65}$$

The effect of imposing continuity of particle displacement along the vortex sheets can be discovered by eliminating η in equations (52 a, b) and taking the half Fourier transform. Addition and subtraction of the results lead to the two relations

$$(1 + M\alpha)S_+^{(o)'} = S^{(i)'} + S^{(V)'} \tag{66a}$$

$$(1 + M\alpha)D_+^{(o)'} = D^{(i)'} + D^{(V)'}, \tag{66b}$$

wherein we used equation (65).

The final set of conditions is found by defining the half Fourier transform of the pressure jump across each of the duct elements:

$$F(\alpha, \pm b) = \int_{-\infty}^{\infty} \{\phi(x_1, \pm b\pm) - [1 + (\mathrm{i}M/k)\frac{\partial}{\partial x_1}]\phi(x_1, \pm b\mp)\}\mathrm{e}^{ik\alpha x_1}\, dx_1 \tag{67}$$

Integrate and take the sum and difference to obtain

$$S_-^{(F)} = \quad S^{(o)} - (1 + M\alpha)\left(S^{(i)} + S^{(V)}\right) \tag{68a}$$

$$D_-^{(F)} = \quad D^{(o)} - (1 + M\alpha)\left(D^{(i)} + D^{(V)}\right). \tag{68b}$$

Due to the continuity of pressure along the vortex sheets, equation (51), it is clear that $F(\alpha, \pm b)$ is analytic in $R_{(-)}$. Consequently, we have added the minus subscript to $S^{(F)}$ and $D^{(F)}$ above. This concludes the formulation stage of the Wiener-Hopf problem. Below we proceed to solve it.

Equations (62a, 64a, 66a, and 68b) are seen to constitute one set of four equations involving the five unknowns $D^{(o)}$, $D^{(i)}$, $S_+^{(o)'}$, $S^{(i)'}$, and $D_-^{(F)}$, and the knowns $D^{(V)}$ and $S^{(V)'} = -k\varpi D^{(V)}$. Equations (62b, 64b, 66b, and 68a) constitute another set involving the unknowns $S^{(o)}$, $S^{(i)}$, $D_+^{(o)'}$, $D^{(i)'}$, and $S_-^{(F)}$, and the knowns $S^{(V)}$ and $D^{(V)'} = -k\varpi S^{(V)}$. Each set of equations leads to a Wiener-Hopf equation, which when split supply the missing relation.

Straightforward algebraic manipulations of the above relations lead to the following set of Wiener-Hopf equations:

$$Y(\alpha)S_+^{(o)'} = -kD_-^{(F)} - k(1 + M\alpha)D^{(V)}[1 + \tanh kb\varpi] \tag{69a}$$

$$Z(\alpha)D_+^{(o)'} = -kS_-^{(F)} - k(1 + M\alpha)S^{(V)}[1 + \coth kb\varpi]. \tag{69b}$$

Kernels $Y(\alpha)$ and $Z(\alpha)$ that appear above are defined by the relations

$$Y(\alpha) = \frac{1}{\gamma} + \frac{(1 + M\alpha)^2 \tanh kb\varpi}{\varpi} \tag{70a}$$

$$Z(\alpha) = \frac{1}{\gamma} + \frac{(1 + M\alpha)^2 \coth kb\varpi}{\varpi}. \tag{70b}$$

To make progress, we need estimates of the various terms in the above equations as $|\alpha| \to \infty$ in the strip, which in turn correspond to certain physical properties as $x_1 \to 0$. According to the full Kutta condition, displacement of the vortex sheet behaves as $\eta(x_1, \pm b) \sim x_1^{3/2}$ as $x_1 \to 0+$. This requires that both $S_+^{(o)'}$ and $D_+^{(o)'}$ behave as $O(\alpha^{-5/2})$ as $|\alpha| \to \infty$ in the positive half plane. The requirement that pressure on the duct be finite leads to the conclusion that $D_-^{(F)}$ and $S_-^{(F)}$ are of order $O(\alpha^q)$ as $|\alpha| \to \infty$ in the negative half plane with $q < 1$.

As noted by Munt [16] and others, the vortex layer in a linear model such as this has an inherent instability, which grows exponentially rapidly downstream. Associated with this instability are zeros of the kernels Y and Z, which are located respectively, say, at $u_0^{(Y)}$ and

$u_0^{(Z)}$ in the complex α plane. The exact location of these zeros depend upon k; for real positive k they are located in the region $\Re\alpha < 0$ and $\Im\alpha > 0$. (Here, $\Im$ is the imaginary operator.) A numerical investigation revealed these zeros were nearly stationary when δ is varied over the range $0 < \delta \leq \pi/2$; furthermore, they were always located in the second quadrant of the complex plane, which we henceforth assume to always be true.

The next step in the Wiener-Hopf procedure is to split the kernel functions as $Y(\alpha) = Y_+(\alpha)Y_-(\alpha)$ and $Z(\alpha) = Z_+(\alpha)Z_-(\alpha)$ with the plus and minus functions regular and non-zero in the respective half planes. If δ is nearly zero, one can deduce that $Y_\pm$ and $Z_\pm$ behave as $O(\alpha^{1/2})$ as $|\alpha| \to \infty$ in the respective half planes. However, if $\delta = \pi/2$, the respective instability zeros become part of Y_+ and Z_+. Then Y_+ and Z_+ are $O(\alpha^{3/2})$ and Y_- and Z_- are $O(\alpha^{-1/2})$ in the respective half planes as $|\alpha| \to \infty$.

To impose causality [16, 21], we set $\delta = \pi/2$ and assume the latter split of the kernels. Rearrangement of the two Wiener-Hopf equations then leads to the following:

$$Y_+ S_+^{(o)'} - J_+ = J_- - \frac{kD_-^{(F)}}{Y_-} \tag{71a}$$

$$Z_+ D_+^{(o)'} - K_+ = K_- - \frac{kS_-^{(F)}}{Z_-} \tag{71b}$$

The new functions appearing above are defined via

$$\begin{aligned} J(\alpha|\mathbf{y}) &= \frac{-k(1+M\alpha)D^{(V)}(\alpha|\mathbf{y})(1+\tanh kb\varpi)}{Y_-(\alpha)} \\ &= J_+(\alpha|\mathbf{y}) + J_-(\alpha|\mathbf{y}) \end{aligned} \tag{72a}$$

and

$$\begin{aligned} K(\alpha|\mathbf{y}) &= \frac{-k(1+M\alpha)S^{(V)}(\alpha|\mathbf{y})(1+\coth kb\varpi)}{Z_-(\alpha)} \\ &= K_+(\alpha|\mathbf{y}) + K_-(\alpha|\mathbf{y}). \end{aligned} \tag{72b}$$

Here we indicate for future reference the dependence upon source location $\mathbf{y}$ through the free-space Green's function $V(x_2|\mathbf{y})$.

The left-hand sides of the two equations appearing in (71) are analytic in the plus half plane, and from the previous estimates, together with the evident smallness of $J_\pm$ and $K_\pm$, vanish in the limit as $|\alpha| \to \infty$. Similarly, the right-hand sides are analytic in the minus half plane and vanish as $|\alpha| \to \infty$. Due to the existence of an overlap region, the two functions must be analytic continuations of each other. Moreover, application of Liouville's theorem leads to the conclusion that both entire functions are identically zero. Thus we obtain the results

$$S_+^{(o)'}(\alpha|\mathbf{y}) = \frac{J_+(\alpha|\mathbf{y})}{Y_+} \tag{73a}$$

$$D_+^{(o)'}(\alpha|\mathbf{y}) = \frac{K_+(\alpha|\mathbf{y})}{Z_+} \tag{73b}$$

The inversion formula for $x_2 > b$ then leads to the expression

$$\mathcal{L}G(\mathbf{x}|\mathbf{y}) = \frac{-i\rho_0 k c_0}{4\pi} \int_\Gamma \frac{1}{\gamma} \left(\frac{J_+(\alpha|\mathbf{y})}{Y_+(\alpha)} + \frac{K_+(\alpha|\mathbf{y})}{Z_+(\alpha)} \right) e^{-ik\alpha x_1 - k\gamma(x_2-b)} \, d\alpha, \tag{74}$$

with the contour Γ a straight line defined via $\Gamma : \alpha = ue^{-i\delta}$ with $-\infty < u < \infty$ (see Fig. 3) and $\delta = \pi/2$.

We obtain the causal result for k real and positive by analytic continuation of the above formula. However, as δ is decreased from $\pi/2$ to 0, the contour Γ crosses the instability zeros of Y_+ and of Z_+. A residue term must be added to the result of the above integration for each of the two instability zeros whenever the contour lies on the other side of the respective zeros; thus for $\delta = 0$, the above formula must be supplemented by two instability terms. If these instability terms are not added, the resulting expression will not satisfy the boundary condition on the duct.

Our interest centers upon the far-field, and there the instability waves are exponentially large near the downsteam axis, particularly for polar angles θ less than approximately 45° (See Appendix A for an investigation of the zeros of the kernels, which are related to the questions of causality and instabilities) as measured from the jet axis. There are various physical mechanisms not represented in the present linear model that will moderate the waves in this region. To make progress, we ignore the instability waves and limit our attention to predictions of the spectral density of the intensity for values of θ greater than either angle associated with the instabilities. For this limited region, equation (74) with $\delta = 0$ is valid.

We can apply the method of stationary phase to evaluate the integral in equation (74) for large distances from the origin. Before doing so, however, it is useful to make the instability zeros explicit and to express the kernel factors in terms of factors that arise from integration along the real axis. First, consider once again $\delta = \pi/2$ and make the instability zeros explicit by writing $Y(\alpha) = (\alpha - u_0^{(Y)})(\alpha - s_0^{(Y)})\hat{Y}(\alpha)$ and similarly for Z. Here, $s_0^{(Y)}$ is a second zero that exists in the cut plane, and equals the complex conjugate of $u_0^{(Y)}$ when $\delta = \pi/2$. This new kernel $\hat{Y}(\alpha)$ could be factored in a straightforward manner by integration over the vertical contour. (See Appendix B for a discussion of factorization of the kernels.) Now both zeros lie in the minus half plane, and thus must belong to Y_+. Hence we may write $Y_+(\alpha) = (\alpha - u_0^{(Y)})(\alpha - s_0^{(Y)})\hat{Y}_+(\alpha)$ and $Y_-(\alpha) = \hat{Y}_-(\alpha)$. A similar factorization exists for Z.

Next, suppose $\delta = 0+$. In this case, the contour Γ collapses onto the real axis, passing above the negative real axis and the branch point at $\alpha = -1$, and below the branch point at $\alpha = 1$ and the positive real axis. In the process of decreasing δ from $\pi/2$ to 0, the zero at $u_0^{(Y)}$ remains almost stationary, but the zero $s_0^{(Y)}$ that was originally located at $u_0^{(Y)^*}$ migrates to $\alpha = -2/M - i0$; this zero thus remains part of the minus analytic plane. If we designate the factorization along this contour with tildes, i.e., $Y(\alpha) = \tilde{Y}_+(\alpha)\tilde{Y}_-(\alpha)$, it clearly follows that $Y_+(\alpha) = (\alpha - u_0^{(Y)})\tilde{Y}_+(\alpha)$ and $Y_-(\alpha) = \tilde{Y}_-(\alpha)/(\alpha - u_0^{(Y)})$, with similar results for Z.

To apply the method of stationary phase, we define polar coordinates (r, θ) (See Fig. 4.) via the relations $x_1 = r\cos\theta$ and $x_2 - b = r\sin\theta$, and initially limit θ to the range $0 < \theta < \pi$. Deform the contour by setting $\alpha = -\cos(\theta + i\tau)$ with $-\infty < \tau < \infty$. The new contour is a branch of an hyperbola, and the deformation does not cross the branch points at $\alpha = \pm 1$. Ignoring any pole or other possible branch point contributions, the method [20]

gives for $kr \to \infty$

$$\mathcal{L}G(\mathbf{x}|\mathbf{y}) \sim \rho_0 c_0 \left(\frac{k}{8\pi r \mathrm{i}}\right)^{1/2} \left(\frac{J_+(\alpha|\mathbf{y})}{(\alpha - u_0^{(Y)})\tilde{Y}_+(\alpha)} + \frac{K_+(\alpha|\mathbf{y})}{(\alpha - u_0^{(Z)})\tilde{Z}_+(\alpha)}\right) \mathrm{e}^{\mathrm{i}kr} \tag{75}$$

with $\alpha = -\cos\theta$. Explicit expressions for J_+ and K_+ are derived in the next subsection from equation (72) with $Y_-(\alpha)$ and $Z_-(\alpha)$ replaced by $\tilde{Y}_-(\alpha)/(\alpha - u_0^{(Y)})$ and $\tilde{Z}_-(\alpha)/(\alpha - u_0^{(Z)})$, respectively.

We now consider possible residue and branch point contributions to $\mathcal{L}G$ in the far field. Aside from poles due to the instability zeros and the branch point at $\alpha = 1$, the integrand is free of singularities in the upper plane. The possible contribution of instability zeros is discussed below. The branch point is not crossed in the deformation, and thus cannot contribute to the integral. It is shown in the next subsection that the only singularities of J_+ and K_+ in the minus analytic region are simple poles at the zeros of $\cosh kb\varpi$ and $\sinh kb\varpi$, respectively; K_+ also possess a simple pole at α_L. However, $\tilde{Y}_+$ and $\tilde{Z}_+$ possess the identical respective poles, and hence these poles cancel. As in the upper plane, the branch point at $\alpha = -1$ is not crossed in the deformation, and may thus be dropped from further consideration. The only remaining possible singularities of the integrand are due to zeros of $\tilde{Y}_+$ and $\tilde{Z}_+$ in the lower plane. There are in fact an infinite number of these zeros, but each gives rise to an exponentially small residue term in the far field. Prior investigators, e.g., Munt [16], have shown that the sum of these terms is negligible compared to the dominant contribution given above.

Consider the possible contribution of the instability zeros to the above integral. In particular, we wish to precisely define the region of the instability wave. Set

$$u_0^{(Y)} = -\cos(\theta_0^{(Y)} + \mathrm{i}\tau_0^{(Y)}) \tag{76a}$$

and

$$u_0^{(Z)} = -\cos(\theta_0^{(Z)} + \mathrm{i}\tau_0^{(Z)}), \tag{76b}$$

where $u_0^{(Y)}$ and $u_0^{(Z)}$ are the locations of the instability zeros when $\delta = 0$. It follows that the instability wave may be neglected relative to the contribution in equation (75) provided θ is greater than the larger of $\theta_0^{(Y)}$ and $\theta_0^{(Z)}$ (which as stated previously are each approximately 45°).

Equation (75) represents a formal solution to the far-field Green's function $\mathcal{L}G$ that appears in the expression $\tilde{\mathbf{G}} = \nabla\nabla\mathcal{L}G$ (equation (46)). Successful use of this solution to predict the spectral density of the intensity requires several more steps, which are described in the next subsection.

3.3 Spectral Density for a Source Located Inside the Duct

We here use the above formal result for $\mathcal{L}G$ to derive an explicit expression for the spectral density of the intensity of sound in the far-field due to isotropic turbulence located at various positions within the duct. The primary steps needed to complete this task are

1. Factorize Y and Z

2. Decompose J and K

3. Evaluate "Correlation Integral"

By "correlation integral", we mean the integration involving the correlation scale $L(\mathbf{y},\tau)$ over the variable τ that appears in equation (45).

Factorization of the kernels is by far the most difficult of these steps. Provided a kernel, say, $\mathcal{Y}(\alpha)$, is regular and nonzero within the strip, and it possesses the proper asymptotic behavior, the corresponding factor $\mathcal{Y}_+$ is given [20] by the expression

$$\ln \mathcal{Y}_+(\alpha) = \frac{1}{2\pi \mathrm{i}} \int_{-\infty+\mathrm{i}0}^{\infty-\mathrm{i}0} \frac{\ln \mathcal{Y}(z)\, dz}{z-\alpha}, \tag{77}$$

for $\delta \to 0+$. The path of integration here is above the negative real axis, below the point α, and below the positive real axis. All singularities along the real axis must be assigned to either the upper or lower planes. The path of integration is then modified to pass either below or above, respectively, the singularity as displayed in Fig. 5. To avoid distracting the reader at this point of the analysis, we consider properties of the kernels and their detailed factorization in two separate appendices. In Appendix A we investigate the zeros of the kernels, and in Appendix B we consider a practical method to factorize them. In any case, the kernel factors are most conveniently calculated numerically. We here assume the kernel factors are available, and move on to consider the decomposition of J and K.

The first step in decomposing J and K is to demonstrate that these two functions are regular at the branch points of ϖ, namely, α_L and α_U. To show this, form the sum and difference of $V(b)$ and $V(-b)$ to obtain $S^{(V)}$ and $D^{(V)}$, respectively, and substitute the results into equation (72). Upon expressing the hyperbolic tangent and cotangent functions in terms of exponentials, we obtain

$$J(\alpha) = \frac{(\alpha - u_0^{(Y)}) \exp(\mathrm{i}k\alpha y_1)}{\mathrm{i}kc_0\rho_0 \tilde{Y}_-(\alpha)} \frac{\sinh k\varpi y_2}{\varpi \cosh kb\varpi} \tag{78a}$$

$$K(\alpha) = \frac{(\alpha - u_0^{(Z)}) \exp(\mathrm{i}k\alpha y_1)}{\mathrm{i}kc_0\rho_0 \tilde{Z}_-(\alpha)} \frac{\cosh k\varpi y_2}{\varpi \sinh kb\varpi}. \tag{78b}$$

These expressions clearly show that the only branch point of J and K is that associated with the kernel factors $\tilde{Y}_-$ and $\tilde{Z}_-$, namely the point $\alpha = 1$.

Decomposition of these functions is accomplished via use of a formula similar to that used for factorizations. For J_+ we have

$$J_+(\alpha) = \frac{1}{2\pi \mathrm{i}} \int_{-\infty+\mathrm{i}0}^{\infty-\mathrm{i}0} \frac{J(z)\, dz}{z-\alpha}, \tag{79}$$

with an equivalent formula for K_+. For a source located within the duct ($y_1 < 0$), the contour may be closed over the lower half plane, and the integral evaluated using Cauchy's integral formula. Summing over the residues yields

$$J_+(\alpha) = \frac{-\mathrm{i}}{k^2 bc_0\rho_0(1-M^2)} \sum_{n=1}^{\infty} \frac{(-1)^n(\alpha_{n-(1/2)}^{(-)} - u_0^{(Y)}) \exp(\mathrm{i}k\alpha_{n-(1/2)}^{(-)} y_1) \sin\left[\frac{(2n-1)\pi y_2}{2b}\right]}{\tilde{Y}_-(\alpha_{n-(1/2)}^{(-)})(\alpha_{n-(1/2)}^{(-)} - \bar{\alpha})(\alpha_{n-(1/2)}^{(-)} - \alpha)} \tag{80a}$$

and

$$K_+(\alpha) = \frac{\mathrm{i}}{k^2 b c_0 \rho_0}\left[\frac{-(\alpha_0^{(-)} - u_0^{(Z)})\exp(\mathrm{i}k\alpha_0^{(-)}y_1)}{2\tilde{Z}_-(\alpha_0^{(-)})(\alpha_0^{(-)}-\alpha)} + \right.$$
$$\left.\frac{1}{1-M^2}\sum_{n=1}^{\infty}\frac{(-1)^n(\alpha_n^{(-)} - u_0^{(Z)})\exp(\mathrm{i}k\alpha_n^{(-)}y_1)\cos n\pi y_2/b}{\tilde{Z}_-(\alpha_n^{(-)})(\alpha_n^{(-)}-\bar{\alpha})(\alpha_n^{(-)}-\alpha)}\right] \quad (80b)$$

Here,

$$\bar{\alpha} = \frac{1}{2}(\alpha_L + \alpha_U) = \frac{M}{1-M^2} \quad (81)$$

represents the midpoint between the two branch points of ϖ. The set of points $\alpha_\nu^{(-)}$ represents the zeros of $\varpi\sinh(kb\varpi)$ and of $\cosh(kb\varpi)$ in the lower-half plane:

$$\alpha_\nu^{(-)} = \begin{cases} \bar{\alpha} - \frac{\mathrm{i}}{kb(1-M^2)}\sqrt{\nu^2\pi^2(1-M^2) - k^2b^2} & \text{for } \nu \geq kb/(\pi\sqrt{1-M^2}) \\ \bar{\alpha} - \frac{1}{kb(1-M^2)}\sqrt{k^2b^2 - \nu^2\pi^2(1-M^2)} & \text{for } \nu \leq kb/(\pi\sqrt{1-M^2}) \end{cases} \quad (82)$$

Here, $\nu = 0,\ 1,\ 2, \ldots$ for zeros of $\varpi\sinh(kb\varpi)$ and $\nu = \frac{1}{2},\ \frac{3}{2},\ \frac{5}{2}, \ldots$ for zeros of $\cosh(kb\varpi)$. Observe that $\alpha_0^{(-)} \equiv \alpha_L$. Values of $\mathcal{L}G$ in the far field can now be determined from knowledge of the kernel factors together with the above expressions for J_+ and K_+.

Due to the exponential dependence upon y_1 in both J_+ and K_+, every term of $\tilde{\mathbf{G}} = \nabla\nabla\mathcal{L}G$ has this same dependence, and this fact along with the form of the turbulence correlation found by Chu [18] for $L(\mathbf{y},\tau)$ permits an exact evaluation of the "correlation" integral.

To make progress in the following, we make this dependence upon y_1 explicit by writing $\nabla\nabla J_+(\alpha|\mathbf{y})$ and $\nabla\nabla K_+(\alpha|\mathbf{y})$ as

$$\nabla\nabla J_+(\alpha|\mathbf{y}) = \sum_{n=1}^{\infty}\mathbf{B}_{n-(1/2)}(\alpha)\exp(\mathrm{i}k\alpha_{n-(1/2)}^{(-)}y_1) \quad (83a)$$

$$\nabla\nabla K_+(\alpha|\mathbf{y}) = \sum_{n=0}^{\infty}\mathbf{B}_n(\alpha)\exp(\mathrm{i}k\alpha_n^{(-)}y_1). \quad (83b)$$

The $\mathbf{B}_\nu(\alpha)$ are independent of y_1 and are easily determined from the above equations. In particular, if we define the set of dyadics $\mathbf{F}_\nu$ as

$$\mathbf{F}_\nu = \exp(-\mathrm{i}k\alpha_\nu^{(-)}y_1)b^2\nabla\nabla\exp(\mathrm{i}k\alpha_\nu^{(-)}y_1)\sin(\nu\pi y_2/b) \quad (84a)$$

for $\nu = n - (1/2)$ with $n = 1, 2, 3, \ldots$, and

$$\mathbf{F}_\nu = \exp(-\mathrm{i}k\alpha_\nu^{(-)}y_1)b^2\nabla\nabla\exp(\mathrm{i}k\alpha_\nu^{(-)}y_1)\cos(\nu\pi y_2/b) \quad (84b)$$

for $\nu = n = 0,\ 1,\ 2, \ldots$, the $\mathbf{B}_\nu(\alpha)$ may be expressed by the equations

$$\mathbf{B}_0(\alpha) = \frac{-\mathrm{i}(\alpha_0^{(-)} - u_0^{(Z)})\mathbf{F}_0}{2k^2b^3c_0\rho_0(\alpha_0^{(-)}-\alpha)\tilde{Z}_-(\alpha_0^{(-)})} \quad (85a)$$

for $\nu = 0$,

$$\mathbf{B}_\nu(\alpha) = \frac{-\mathrm{i}(-1)^{(\nu+(1/2))}(\alpha_\nu^{(-)} - u_0^{(Y)})\mathbf{F}_\nu}{k^2 b^3 c_0 \rho_0 (1-M^2)\tilde{Y}_-(\alpha_\nu^{(-)})(\alpha_\nu^{(-)} - \bar{\alpha})(\alpha_\nu^{(-)} - \alpha)} \tag{85b}$$

for $\nu = n - (1/2)$, $n = 1,\ 2,\ 3, \ldots$, and

$$\mathbf{B}_\nu(\alpha) = \frac{\mathrm{i}(-1)^{\nu}(\alpha_\nu^{(-)} - u_0^{(Z)})\mathbf{F}_\nu}{k^2 b^3 c_0 \rho_0 (1-M^2)\tilde{Z}_-(\alpha_\nu^{(-)})(\alpha_\nu^{(-)} - \bar{\alpha})(\alpha_\nu^{(-)} - \alpha)} \tag{85c}$$

for $\nu = n = 1,\ 2,\ 3, \ldots$. To complete the definition of $\mathbf{B}_\nu(\alpha)$, we give explicit expressions for $\mathbf{F}_\nu$:

$$\begin{aligned}\mathbf{F}_\nu = &-\mathbf{i}_1\mathbf{i}_1 k^2 b^2 \alpha_\nu^{(-)^2} \sin(\nu\pi y_2/b) + \\ &(\mathbf{i}_1\mathbf{i}_2 + \mathbf{i}_2\mathbf{i}_1)\mathrm{i}kb\alpha_\nu^{(-)}\nu\pi\cos(\nu\pi y_2/b) - \mathbf{i}_2\mathbf{i}_2\nu^2\pi^2\sin(\nu\pi y_2/b)\end{aligned} \tag{86a}$$

for $\nu = n - (1/2)$ with $n = 1, 2, 3, \ldots$, and

$$\begin{aligned}\mathbf{F}_\nu = &-[\mathbf{i}_1\mathbf{i}_1 k^2 b^2 \alpha_\nu^{(-)^2} \cos(\nu\pi y_2/b) + \\ &(\mathbf{i}_1\mathbf{i}_2 + \mathbf{i}_2\mathbf{i}_1)\mathrm{i}kb\alpha_\nu^{(-)}\nu\pi\sin(\nu\pi y_2/b) + \mathbf{i}_2\mathbf{i}_2\nu^2\pi^2\cos(\nu\pi y_2/b)]\end{aligned} \tag{86b}$$

for $\nu = n = 0,\ 1,\ 2, \ldots$. It then follows from equation (75) that $\tilde{\mathbf{G}}$ may be written as

$$\tilde{\mathbf{G}} \sim \rho_0 c_0 \left(\frac{k}{8\pi r\mathrm{i}}\right)^{1/2} \mathrm{e}^{\mathrm{i}kr}\left(\frac{\sum_{n=1}^{\infty}\mathbf{B}_{n-(1/2)}\exp(\mathrm{i}k\alpha_{n-(1/2)}^{(-)}y_1)}{(\alpha - u_0^{(Y)})\tilde{Y}_+(\alpha)} + \frac{\sum_{n=0}^{\infty}\mathbf{B}_n\exp(\mathrm{i}k\alpha_n^{(-)}y_1)}{(\alpha - u_0^{(Z)})\tilde{Z}_+(\alpha)}\right) \tag{87}$$

with $\alpha = -\cos\theta$ for $kr \to \infty$.

Let $\mathcal{G}^T$ be the so-called correlation integral. For convenience, we here define the complex conjugate of the correlation integral as (compare with equation (45))

$$\mathcal{G}^{T^*} = \int_{-\infty}^{\infty} \mathrm{e}^{\mathrm{i}\omega\tau}\tilde{\mathbf{G}}(\mathbf{x}|\mathbf{y} + \mathbf{i}_1 U_c\tau)L(\mathbf{y},\ \tau)\ d\tau, \tag{88}$$

and following integration take the complex conjugate to get $\mathcal{G}^T$. From the above expression for $\tilde{\mathbf{G}}$, it is clear the typical scalar integral I_ν is of the form

$$I_\nu = \int_{-\infty}^{\infty} \mathrm{e}^{\mathrm{i}\omega\tau(1+M_c\alpha_\nu^{(-)})}L(\mathbf{y},\tau)\ d\tau. \tag{89}$$

Repeated integration by parts leads to

$$I_\nu = \frac{1}{\omega^4(1+M_c\alpha_\nu^{(-)})^4}\int_{-\infty}^{\infty}\mathrm{e}^{\mathrm{i}\omega\tau(1+M_c\alpha_\nu^{(-)})}\frac{\partial^4 L}{\partial\tau^4}\ d\tau \tag{90}$$

Chu [18] experimentally measured the two-point space-time correlations of both the turbulent velocities and the squares of these velocities in the mixing region of a 4-inch circular jet for low subsonic Mach numbers. The experiments showed that the fourth derivative of the relevant "self-noise" data could be fit well with analytical functions of the type

$$\frac{\partial^4 L}{\partial\tau^4} = L_0^{(IV)}\ \mathrm{sech}\ (\omega_f\tau)\cos(\omega_*\tau), \tag{91}$$

with $L_0^{(IV)}$, ω_f, ω_* experimentally-determined constants. Unlike the conditions of Chu's experiments, the present model assumes a planar jet within a two-dimensional space. Perhaps most significantly, turbulent fluctuations are here constrained to lie within the two-dimensional space. However, for lack of better information, we will use these results in the present theory. Introduction of Chu's expression into equation (90) followed by a standard integration leads to

$$I_\nu = \frac{\pi L_0^{(IV)}}{2k_f k^4 c_0^5 (1+M_c\alpha_\nu^{(-)})^4}\left\{\text{sech}\left[\frac{\pi[(1+M_c\alpha_\nu^{(-)})k+k_*]}{2k_f}\right]+ \text{sech}\left[\frac{\pi[(1+M_c\alpha_\nu^{(-)})k-k_*]}{2k_f}\right]\right\}, \tag{92}$$

where $k_f = \omega_f/c_0$ and $k_* = \omega_*/c_0$ are wavenumbers corresponding to the respective frequency parameters.

The above result leads directly to the expression for $\mathcal{G}^T$:

$$\mathcal{G}^T \sim \left\{\rho_0 c_0\left(\frac{k}{8\pi r\mathrm{i}}\right)^{1/2} \mathrm{e}^{\mathrm{i}kr}\left(\frac{\sum_{n=1}^{\infty}\mathbf{B}_{n-(1/2)}I_{n-(1/2)}\exp(\mathrm{i}k\alpha_{n-(1/2)}^{(-)}y_1)}{(\alpha-u_0^{(Y)})\tilde{Y}_+(\alpha)}+ \frac{\sum_{n=0}^{\infty}\mathbf{B}_n I_n\exp(\mathrm{i}k\alpha_n^{(-)}y_1)}{(\alpha-u_0^{(Z)})\tilde{Z}_+(\alpha)}\right)\right\}^* \tag{93}$$

with $\alpha = -\cos\theta$ for $kr \to \infty$.

Our explicit expression for the spectral density of the intensity in the far-field follows from equation (45) and the above results. Specifically, we find

$$I_\omega(\mathbf{x}|\mathbf{y}) \sim \frac{7\rho_0\left(\overline{u^2}\right)^2}{8\pi c_0}\Re\left(\frac{1}{7}\tilde{G}_{ii}\mathcal{G}_{jj}^T + \tilde{G}_{ij}\mathcal{G}_{ij}^T\right). \tag{94}$$

in Cartesian tensor notation. The above expression is used in the next section to predict the directivity for selected values of frequency, Mach number, and source location.

4 Discussion of Results

We discuss various aspects of the theory just derived to give insight into the graphical results that follow. A small subsection then gives suggestions for future work.

Each term in equation (80) corresponds to a different mode of wave propagation within the duct, and hence represents the contribution of that mode to the far-field Green's function $\mathcal{L}G$. According to equation (82), only certain $\alpha_\nu^{(-)}$ will be real, and the number of real $\alpha_\nu^{(-)}$ increases with frequency kb; these correspond to traveling waves within the duct. Note that the associated terms in equation (80) are not exponentially damped in the far-field expression for $\mathcal{L}G$ and similarly for I_ω. Also note that at sufficiently low frequencies, $\alpha_0^{(-)}$ is the only real $\alpha_\nu^{(-)}$; this term corresponds to plane wave propagation within the duct.

All other $\alpha_\nu^{(-)}$ will have a negative imaginary part. The corresponding terms in equation (80) ultimately make exponentially small contributions of order $\exp(-k|y_1\Im\,\alpha_\nu^{(-)}|)$ to $\mathcal{L}G$

and a similar small contribution to I_ω. Here, $\Im$ denotes the imaginary operator. Note that as a source is moved upstream within the duct, these factors decrease rapidly with distance, so that for a source located sufficiently far upstream, only terms consisting of real $\alpha_\nu^{(-)}$, i.e., the traveling modes, will to contribute to the sum. On the other hand, for a source located near the end of the duct, several terms with complex $\alpha_\nu^{(-)}$ will contribute to the far-field, but the magnitude of each successive term will decrease exponentially rapidly. These terms can be associated with acoustic waves that cannot propagate within the duct due to their wavelength being too large. However, if the turbulent source is located sufficiently near the end of the duct, some of these waves may escape to the far-field.

The case where the source is located at dead center ($y_2 = 0$) is of particular interest. For a source locate there, only symmetric ($\nu = n$) modes modes contribute to $\mathcal{L}G$ in the far field. However, both symmetric and asymmetric ($\nu = n - 1/2$) modes still generally contribute to the far-field intensity because it depends upon $\nabla\nabla\mathcal{L}G$.

We now use the preceding theory to predict typical directivities of the far-field intensity due to sound emitted from a unit volume of turbulence within the duct. Frequency and source position are the primary parameters varied in this study. Before proceeding, specific values are required for the turbulence correlation parameters k_f and k_* that appear within equation (91) for the turbulent source. According to Chu [18], the data are best fit with the choices

$$\begin{aligned} b_0 k_f &= 2.3 M_e \\ b_0 k_* &= 5.4 M_e \end{aligned}$$

for a cylindrical jet of radius b_0 and exit Mach number M_e. We accept these relations even for our two-dimensional space, and consider b_0/b as a geometric ratio (the "radius ratio") with a value near unity that can be varied to some extent. Also appearing in our expression for the spectral density is the eddy convection Mach number M_c. We here assume the relation

$$M_c = \frac{1}{2} M.$$

Goldstein and Rosenbaum [12] suggested that it may be suitable to take M_c as the negative of that given above to model sound emitted from the entrance of a jet as in an augmentor flap; for this purpose, they principally employed a radius ratio of 0.25. As might be expected, they suggest a radius ratio of unity to model the sound emitted from the rear of the flap. In any case, different physical geometries might suggest the use of different values of this ratio. For our purposes, we take M_c as positive, and use 0.25 and unity for the radius ratio to test the sensitivity of results to this parameter.

The remaining parameters requiring selection are the Mach number M, the frequency parameter kb, and the source location (y_1, y_2). Chu's data was collected for low subsonic Mach numbers, and so we set $M = 0.3$ in all our examples. We consider three different frequencies, low, low intermediate, and high: $kb = 0.25\pi$ (wavelength $\lambda = 8b$), 0.75π ($\lambda = 2.67b$), and $kb = 6\pi$ ($\lambda = 0.33b$). For the lowest frequency, $\alpha_0^{(-)}$ is the only real $\alpha_\nu^{(-)}$. For the next frequency, $\alpha_{1/2}^{(-)}$ is also real. For the highest frequency, the real $\alpha_\nu^{(-)}$ correspond to $\nu = 0,\ 1/2,\ 1,\ \ldots,\ 6$. Based upon the full duct width, these frequencies correspond to Strouhal numbers $(\omega/2\pi)2b/U$ of 0.83, 2.5, and 20, respectively. Finally, we assume the

source is located at various vertical positions near the end of the duct. More precisely, we set $y_1 = -b$, and present results for a source located near the lower wall ($y_2 = -0.875b$), in the center between the two walls ($y_2 = 0$), and near the upper wall ($y_2 = 0.875b$).

We plot a scaled spectral density of the intensity $\hat{I}_\omega$:

$$\hat{I}_\omega(\mathbf{x}|\mathbf{y}) = \frac{128 r k_f c_0^6 I_\omega(\mathbf{x}|\mathbf{y})}{7\rho_0 \left(\overline{u^2}\right)^2 L_0^{(IV)} b Q}. \tag{96}$$

We inserted a scaling parameter Q above so that the maximum value of $\hat{I}_\omega$ equals 100, thereby aiding comparison of the various results that follow. Figs. 6, 7, and 8 each contain four polar plots of the scaled spectral density. The three figures correspond respectively to the low, low intermediate, and high frequencies mentioned above. The first three plots within each set correspond to a source located near the lower wall, in the center, and near the upper wall. For these plots, the radius ratio equals 0.25. For the final plot of each set, the radius ratio is set to unity for a source located at $(-b,\ 0)$. Thus, comparison of second and fourth plots within each set reveals the sensitivity to the radius ratio. Finally, a dashed line drawn at an angle of 45° also appears within each graph. The area to the right of this line represents the region where the instability wave is exponentially large, but which we choose to ignore in the present solution.

Fig. 6 displays directivities for low-frequency radiation as predicted by the current theory. All four directivity curves are oval in appearance with maximums occurring near 40°. Looking more closely at Figs. 6A, 6B, and 6C, we note that as the source moves from near the lower wall to near the upper, the angle of the maximum increases slightly from 36° to 39°, and the maximum value of the spectral density monotonically decreases only slightly: Q changes from 2.27 (10^{-3}) to 2.07 (10^{-3}). From Figs. 6B and 6D, we note the shape of the directivity curve is nearly unchanged by increasing the radius ratio by a factor of four, but the value of Q more than doubled with this change from 2.18 (10^{-3}) to 5.15 (10^{-3}).

Directivities for our low-intermediate frequency appear in Fig. 7. Despite an increase in the frequency by a factor of three, the gross features of these directivity curves are similar to those of the lower frequency. However, closer examination reveals that many of the trends discovered above no longer hold at this increased frequency. As the source location moves from near the lower plate to near the upper in Figs. 7A, 7B, and 7C, the angle at which the maximum appears *decreases* from 44° to near 40°. Moreover, the maximum values Q of the spectral density in these respective cases are 1.53 (10^{-3}), 1.34 (10^{-3}), and 1.45 (10^{-3}); there is no longer a monotonic decrease in Q as the source moves from the near the lower plate to near the upper. For a source located near the upper plate, Fig. 7C, a lobe appears forming near 60° that is absent is all the previous results. Figs. 7B and 7D suggest that the radius ratio again has little effect upon the shape of the directivity curve. But as in the low-frequency case, Q is sensitive to the radius ratio; it more than triples from 1.34 (10^{-3}) to 4.53 (10^{-3}) when this ratio changes from 0.25 to 1.

Our high-frequency directivity results are displayed in Fig. 8. As at the lower frequencies examined above, the major portion of the radiation in the far-field occurs at angles θ near 40°. For a source located near the lower plate (Fig. 8A), multiple peaks are clearly seen with the magnitude of each subsequent peak decreasing as θ increases. The source located at the center (Fig. 8B) gives rise to a single major peak near 40°. A much smaller peak in the

directivity is observed at an angle near 75°. The source located near the upper plate (Fig. 8C) gives rise to multiple peaks near 40°. These maximums again decrease in magnitude as θ increases, but the angular distance between them are considerably less than for the source located near the lower plate. A minor peak near 80° is observed. In contrast to the lower frequencies examined above, the angle of the primary maximum is here nearly constant (40°), independent of the value of y_2. The values of Q for these curves are 2.55 (10^{-5}), 1.22 (10^{-4}), and 2.81 (10^{-5}), respectively; the trend represented by these Q-values is different than in either of the two preceding cases. Figs. 8B and 8D show two nearly identical directivity curves. However, the value of Q for the case of unit radius ratio is 5.21 (10^{-17}), several orders of magnitude less than the value 1.22 (10^{-4}) found for a radius ratio of 0.25. The sensitivity to this ratio can be traced to the exponential decrease in the values of the hyperbolic secant functions that appear in equation (92), which define the integrals I_ν. High sensitivity of Q to the radius ratio can be expected at high frequencies.

In the limit of zero jet Mach number, the present theory leading to equation (45) for I_ω is equivalent to the expression found by Goldstein and Rosenbaum [12] for the spectral density of "self-noise" intensity in their Lighthill formulation. Goldstein and Rosenbaum went on to apply their theory to a two-dimensional plug flow jet as we have done, except they assumed the resulting waves propagated within a three-dimensional space in contrast to our assumption of a two-dimensional space. Due to this difference in dimensions, it is difficult to quantitatively compare the two theories. Figs. 13a and 13b of Goldstein and Rosenbaum give the directivity of self noise for a source located at (-b,0) for low and high frequencies, respectively. Compared to present results, the directivities of Goldstein and Rosenbaum vary only slightly with the angle of observation from the plane of the jet.

In connection with experimental evidence of the downstream beaming of low frequency radiation [5], we note that Goldstein and Rosenbaum find finite directivities in the limit $\theta \to 0$. In contrast, the present theory indicates that for finite jet Mach numbers the directivity vanishes in this limit, independent of the frequency. This property of the present theory, which is no doubt related to the well-known refraction of waves as they cross a vortex sheet [22], can be deduced from equation (70) and the realization that both $Y_+(\alpha)$ and $Z_+(\alpha)$ must possess the singular behavior $(\alpha + 1)^{-1/2}$ as $\alpha = -\cos\theta \to -1$. Consequently, the inverse of these kernel factors and hence I_ω both vanish in this limit. However, as noted above, the present theory should reduce to the self-noise theory of Goldstein and Rosenbaum in the limit of zero jet Mach number. We should therefore expect that if the limit $M \to 0$ is taken prior to the limit $\theta \to 0$, a finite directivity will result. That this is indeed the case can be seen by noting that the pole of the $Z(\alpha)$ kernel at $\alpha = \alpha_L = \alpha_0^{(-)}$ moves to -1 in this limit. However, according to equation (85a), $\mathbf{B}_0$ will also have a simple pole at $\alpha = -1$. These two singularities will therefore cancel in $\mathbf{B}_0/Z_+$, thereby leading to the conclusion that the present theory predicts a finite directivity along the jet axis in the limit of zero jet Mach numbers.

As noted above, the present model predicts a zone of relative silence near the jet axis for all frequencies, not just for high frequencies as is seen experimentally. Thus, the present model cannot predict the downstream beaming observed by Lush [5] for low-frequency radiation. This failure of our model problem has at least two plausible explanations. One possibility is simply that the region of downstream beaming is also the region of wave instability, and our solution, which excludes this instability wave, is not strictly valid in this region. According

to this view, the directivity of sound within the instability region cannot be known from the present model. A second possibility is that the present model problem, selected for its relative ease in solution, does not capture the important physics that gives rise to the downstream beaming, e.g., the refractive effect of mean-flow shear. Goldstein [9, 10] showed, e.g., that convecting quadrupoles of infinite lifetimes in a free jet give rise to downstream beaming in the low frequency limit; that model predicts that the directivity of pressure in this region is proportional to the gradient of the Mach number at the source location. In the present plug-flow model, there are no gradients of the mean velocity except within the vortex layers, which are effectively of zero thickness. We also precluded sources from being located within such layers. Thus, this possible cause of downstream beaming was eliminated by selecting a plug-flow model.

In this contribution, we have insisted upon satisfying the condition of causality, and this insistence lead to the instability wave and the related question of interpretation within the instability region. We note, however, that Dowling, et al. [23] have argued that causality need not be satisfied in problems of the present type.

Future Work

Our expression for the spectral density of the far-field intensity due to a unit volume of turbulence, equation (45), can be applied to several different geometries and mean velocity profiles. In the present effort, we applied the expression to a two-dimensional duct from which a plug flow jet exits. Below we list possible extensions of the present work.

1. The present study examined only one Mach number and a few frequencies and source positions. Predictions of the model should be extended to a broader range of parameters, and these results should then be compared in detail with prior models and relevant experimental data.

2. Compare predictions of the present two-dimensional space problem with those calculated using a non-causal Green's function.

3. The present plug-flow model is limited to a two-dimensional space. It is anticipated that extension of the model to sound radiation in a three-dimensional space while retaining the two-dimensional duct/jet geometry would give insight into the directivity due to jets passing through narrow slits.

4. Adaptation of this plug-flow model to cylindrical ducts would be helpful.

5. The inclusion of mean flow shear (in whatever geometry it is feasible) would represent a tremendous advance in current understanding.

6. Results of these investigations should be implemented into code (e.g., the MGB code) for the design of actual jets.

5 Summary

Starting from a linearized version of the Lilley equation, we derived an expression for the spectral density of the far-field intensity for sound emitted from a unit volume of turbulence located within a jet and near solid boundaries. The theory is valid for arbitrary unidirectional, transversely sheared mean flows. The theory was applied to a simple two-dimensional jet that exits a relatively long duct. Due to the complexity of the governing equations, a simple plug flow was assumed for the jet. The resulting equations were solved exactly in a formal sense using the Wiener-Hopf technique. Using existing turbulence correlation data, the spectral density was calculated and plotted for a wide range of frequencies and for sources located at various points just inside the duct.

Acknowledgements

The authors express their sincere appreciation to several individuals who made this work possible: to M. Majjigi of GE Aircraft Engines, who defined the problem from an application-oriented perspective; to J. Earls, who was instrumental in initiating the project; to J. Shaw for financial support; and to M. E. Goldstein, who helped define the technical problem and provided invaluable technical assistance. The last three individuals above are employees of the NASA Lewis Research Center. This work was supported by NASA contract NAS3-27571.

References

1. M. J. Lighthill. On sound generated aerodynamically I. general theory. *Proceedings of the Royal Society*, A211:564–587, 1952.

2. M. J. Lighthill. On sound generated aerodynamically II. turbulence as a source of sound. *Proceedings of the Royal Society*, A222:1–32, 1954.

3. Marvin E. Goldstein. *Aeroacoustics*. McGraw-Hill, New York, 1976.

4. G. M. Lilley. Jet noise classical theory and experiments. In Harvey H. Hubbard, editor, *Aeroacoustics of Flight Vehicles: Theory and Practice Volume 1: Noise Sources*, pages 211–289, NASA Reference Publication 1258, 1991.

5. P. A. Lush. Measurements of subsonic jet noise and comparison with theory. *Journal of Fluid Mechanics*, 46:477–500, 1971.

6. G. M. Lilley. *Fourth Monthly Progress Report on contract F-33615-71-C-1663. Appendix: Generation of Sound in a Mixing Region.* Technical Report, Lockheed Aircraft Company, Marrietta, GA, 1971.

7. R. Mani. A moving source problem relevant to jet noise. *Journal of Sound and Vibration*, 25:337–347, 1972.

8. R. Mani. Further studies on moving source solutions relevant to jet noise. *Journal of Sound and Vibration*, 35:101–117, 1974.

9. M. E. Goldstein. The low frequency sound from multipole sources in axisymmetric shear flows, with applications to jet noise. *Journal of Fluid Mechanics*, 70:595–604, 1975.

10. M. E. Goldstein. The low frequency sound from multipole sources in axisymmetric shear flows. Part 2. *Journal of Fluid Mechanics*, 75:17–28, 1976.

11. M. E. Goldstein. High frequency sound emission from moving point multipole sources embedded in arbitrary transversely sheared mean flows. *Journal of Sound and Vibration*, 80:499–522, 1982.

12. Marvin E. Goldstein and Burt M. Rosenbaum. *Emission of Sound from Turbulence Convected by a Parallel Flow in the Presence of Solid Boundaries.* NASA Technical Note D-7118, National Aeronautics and Space Administration, Washington, D.C., 1973.

13. R. Mani. Refraction of acoustic duct waveguide modes by exhaust jets. *Quarterly of Applied Mathematics*, 30:501–521, 1973.

14. S. D. Savkar. Radiation of cylindrical duct acoustic modes with flow mismatch. *Journal of Sound and Vibration*, 42:363–386, 1975.

15. R. M. Munt. Acoustic radiation from a circular cylinder in a subsonic stream. *J. Inst. Math.*, 16:1–10, 1975.

16. R. M. Munt. The interaction of sound with a subsonic jet issuing from a semi-infinite cylindrical pipe. *Journal of Fluid Mechanics*, 83:609–640, 1977.

17. A. M. Cargill. Low-frequency sound radiation and generation due to the interaction of unsteady flow with a jet pipe. *Journal of Fluid Mechanics*, 121:59–105, 1982.

18. Wing T. Chu. *Turbulence Measurements Relevant to Jet Noise.* Technical Report 119, University of Toronto Institute for Aerospace Studies, Toronto, Ontario, 1966.

19. Marvin E. Goldstein and Burt M. Rosenbaum. *Emission of Sound from Axisymmetric Turbulence Convected by a Mean Flow with Application to Jet Noise.* NASA Technical Note TN-6939, National Aeronautics and Space Administration, Washington, D.C., 1972.

20. B. Noble. *Methods Based on the Wiener-Hopf Technique.* Pergamon Press, New York, 1958.

21. D.G. Crighton and F.G. Leppington. Radiation properties of the semi-infinite vortex sheet: the initial-value problem. *Journal of Fluid Mechanics*, 64:393–415, 1974.

22. Philip M. Morse and K. Uno Ingard. *Theoretical Acoustics.* Princeton University Press, Princeton, 1968.

23. A.P. Dowling, J.E. Ffowcs Williams, and M.E. Goldstein. Sound production in a moving stream. *Philosophical Transactions of the Royal Society London*, A288(1353):321–349, 1978.

Appendix A Zeros of Kernels

Due to the need to impose causality, the location of zeros of Y and Z (defined in equation (70)) in the complex plane and their path as certain parameters change play an important role in the present analysis. Where possible, we here employ analytical techniques to investigate the zeros, and, where these fail, indicate suitable numerical procedures. Munt [16] gives an excellent discussion on this topic in connection with a related kernel for cylindrical jets.

For the present kernels, perhaps the most useful information is obtained upon assuming k is pure imaginary, i.e., $\delta = \arg k = \pi/2$. In this case, all poles of Y and Z must lie along the real axis. Therefore, we can employ the argument principle around a large contour in the upper or lower plane to determine whether any zeros are present. Furthermore, the easily proved general identity,

$$Y^*(\alpha,\ k) = -Y(\alpha*,\ -k*), \tag{A.1}$$

is extremely useful. (For this discussion of the kernel zeros, it is useful to consider Y and Z as functions of both α and k.) If k is pure imaginary, for any zero located in the upper complex plane, say, at $\alpha = u_0^{(Y)}$, there must also exist a zero of Y in the lower complex plane at $u_0^{(Y)^*}$. Exactly the same reasoning applies to the kernel Z.

We examined the change in $\arg Y$ and $\arg Z$ along a closed path just above the real axis, say from $-R < \Re\alpha < R$ for large R, and then along the semi-circular contour following the path $\alpha = Re^{i\phi}$ with $0 < \phi \leq \pi$. One can deduce (See Munt [16] for details.) that the change in argument for both kernels is 2π, indicating the presence of one simple zero in the upper plane for each kernel and hence another one at the complex conjugate of this root.

If the roots are located in a region in the complex plane where $2\Re\ kb\varpi >> 1$, then to within an exponentially small order the hyperbolic tangent and cotangent functions may be replaced by unity. To this order of approximation, the two kernels become identical to each other and to the kernel found by Crighton and Leppington [21] for a single semi-infinite vortex sheet. Crighton and Leppington located this zero at

$$u_0 = -\cos(\frac{\pi}{4} + i\tau_0), \tag{A.2}$$

where τ_0 is the positive root of

$$\cosh\tau_0 = [1 + \sqrt{1+M^2}]/\sqrt{2}M \tag{A.3}$$

This zero is located in the second quadrant of the complex plane, and the actual zeros $\alpha = u_0^{(Y)}$ and $\alpha = u_0^{(Z)}$ of the two respective kernels are expected to be located nearby. Since there *must* be a location in the upper complex plane where $2\Re\ kb\varpi >> 1$, it follows that these are the sole zeros in the upper plane indicated by the argument procedure.

Before leaving this case, we note that the above argument procedure did not capture all zeros of Y and Z in the cut plane, for some zeros are possibly located along the real axis between -1 and α_L. The number of zeros in this region increase with the magnitude of kb. There are no other zeros along the real axis.

The above zeros account for all zeros of both kernels in the cut plane when k is pure imaginary. For $\delta = \pi/2$, the contour of integration Γ, used for factorization of the kernels

(See Figure 3.) coincides with the imaginary axis. Thus, all the discovered zeros lie in the minus analytic plane, and are part of the plus kernel factors. It is useful to trace these zeros as δ decreases to zero, and thereby determine whether they become part of the plus analytic region. The trajectory of these zeros can be determined by numerically solving the implicit equation

$$\frac{\partial \alpha}{\partial \delta} = -\frac{\frac{\partial Y}{\partial \delta}}{\frac{\partial Y}{\partial \alpha}}. \tag{A.4}$$

For all cases investigated, we found

1. The zeros at $\alpha = u_0^{(Y)}$ and $\alpha = u_0^{(Z)}$ remained virtually stationary as δ decreased to zero. Therefore, these zeros were crossed by Γ, and are the so-called instability zeros.

2. The zeros initially located at $s_0^{(Y)} = u_0^{(Y)^*}$ and $s_0^{(Z)} = u_0^{(Z)^*}$ for $\delta = \pi/2$ migrated to just below the real axis for $\delta \to 0$. In this limit one can deduce these zeros are located (to within an exponentially small error) at $\alpha = -2/M$. These zeros remain fully within the minus analytic region.

3. The zeros initially located between -1 and α_L appeared to migrate about the point α_L so as to lie fully below the real axis when $\delta = 0$. These zeros thus also remained within the minus analytic region.

We now suppose k is real and positive. Both Y and Z possess an infinite number of poles associated with the zeros of $\cosh kb\varpi$ and $\sinh kb\varpi$, respectively, along the line $\Re\ \alpha = \bar{\alpha}$; they also possess a finite number of poles along the real axis between α_L and α_U.

Now consider the zeros. For $2\Re\ kb\varpi >> 1$, the hyperbolic tangent and cotangent functions may again be replaced by unity. Alternatively, for $-2\Re\ kb\varpi >> 1$, these functions may be replaced by -1. This latter situation occurs in the first and third quadrants relative to an origin at $\alpha = \bar{\alpha}$. The same procedure (rationalization followed by factorization of a sixth-order polynomial) given by Crighton and Leppington [21] can be used to identify all roots satisfying either criteria. Only two of the six polynomial roots are approximate roots of our kernels, and these were identified above: the instability zero at u_0 and the root near $\alpha = -2/M - \mathrm{i}0$.

The other possibility is that $2|\Re\ kb\varpi| \leq O(1)$. This region consists of a strip on either side of the line $\Re\ \alpha = \bar{\alpha}$ and the strip on either side of the real axis between α_L and α_U. It appears that these zeros are interlaced with the poles that occur in these regions.

To more closely investigate these zeros, we factor $\gamma \cosh kb\varpi$ from the denominator to obtain

$$Y = \frac{1}{\gamma \cosh kb\varpi}\left[\cosh kb\varpi + \frac{(1+M\alpha)^2 \gamma \sinh kb\varpi}{\varpi}\right]. \tag{A.5}$$

The quantity in square brackets is suitable for use with the argument method to investigate zeros in the cut plane because it has the same zeros as Y, but none of the poles. Furthermore, the branch point singularities at $\alpha = \pm 1$ are weaker than in Y, which aids implementation of the argument method near these points.

We numerically calculated the change in argument of the quantity above in square brackets along paths surrounding extensive regions of the upper and lower complex planes to determine the precise number of enclosed zeros. The results confirm that the only zeros in the cut plane consist of the instability zero and the zeros associated with poles in the strips mentioned above. The zero near $\alpha = -2/M$ is not captured because it lies on the branch cut. In addition, a finite number of zeros lie along the real axis between 1 and α_U; these are interspersed with poles of Y that lie in this region. Numerical calculations indicate that these zeros move into the other Riemann sheet as δ increases from zero. However, we have not been able to prove in general that this is the case.

These results suggest that each kernel has only one zero, namely, $u_0^{(Y)}$ for the Y kernel and $u_0^{(Z)}$ for the Z kernel, that represents an instability zero. The contour of integration Γ does not appear to cross any other zero when δ varies in the range $0 < \delta \leq \pi/2$. However, since we have not been able to analytically prove this result, an investigation of the zeros of the kernels should be conducted for each new value of kb and M.

Appendix B Numerical Factorization of Kernels

Factorization of kernels tends to be the most difficult aspect of the Wiener-Hopf analysis, particularly if the goal is to obtain analytical expressions. However, the present analysis only requires knowledge of the kernel values at particular points in the complex plane, and for this purpose numerical evaluation of the factors is quite acceptable. In this appendix, we discuss a straightforward and practical approach for the numerical factorization of these kernels. Specific details are given for the factorization of the kernel Y. Factorization of the kernel Z can be treated in a similar manner. We first suppose α lies within the range $-1 < \alpha < 1$, and then later consider the case of complex α.

We begin with equation (77) for the definition of the plus analytic factor $\mathcal{Y}_+(\alpha)$ for the generic kernel $\mathcal{Y} = \mathcal{Y}_+\mathcal{Y}_-$. In using this expression, we assume no zeros exist in the strip and that $\mathcal{Y} \to 1$ as $\alpha \to \infty$ in the strip. Neither Y nor Z, defined in equation (70), satisfy this latter condition, but it is easy to multipy by suitable functions that have known factors and thereby correct this defect. For example, if we define $\mathcal{Y}$ by

$$\begin{aligned} \mathcal{Y} &= \frac{Y\sqrt{1-M^2}}{M^2\gamma} \\ &\equiv \left(\frac{1}{\gamma} + \frac{(1+M\alpha)^2 \tanh kb\varpi}{\varpi}\right)\frac{\sqrt{1-M^2}}{M^2\gamma}, \end{aligned} \tag{B.6}$$

the condition is satisfied. The function γ can be factored as $\gamma_+\gamma_-$ with $\gamma_+(\alpha) = \sqrt{\alpha+1}$ and $\gamma_-(\alpha) = \sqrt{\alpha-1}$. Then suitable factors of $Y = \tilde{Y}_+\tilde{Y}_-$ are $\tilde{Y}_+(\alpha) = M^2\gamma_+(\alpha)\mathcal{Y}_+/\sqrt{1-M^2}$ and $\tilde{Y}_-(\alpha) = \gamma_-(\alpha)\mathcal{Y}_-$. (Recall that we use a tilde to denote the factorization $Y = \tilde{Y}_+\tilde{Y}_-$ along the real axis, and similarly for Z.)

Equation (77) derives (See Noble [20]) from application of Cauchy's integral theorem to a thin rectangular domain that lies within the analytic strip S. The path of integration represents one of the long sides of the rectangle. Because our interest assumes k is real and positive, the limit $\arg k \to 0$ must be taken prior to numerical evaluation. This limiting process causes the kernel $\mathcal{Y}$, which by definition is analytic within the strip (of finite width

when $\arg k > 0$), to appear to have singularities along the path of integration. We have to deal appropriately with these singularities. In particular, it is important to know the locations of the singularities, their type, and which side of the singularities the path of integration follows.

Over the path of integration, different branches of the logarithm function are normally encountered. It is necessary to keep track of these branches during the integration process.

We note certain easily-determined properties of $\mathcal{Y}$ along the path of integration (See Figure 5) for k real and positive. First, $\mathcal{Y}$ is real, positive, and free of singularities for $\alpha < -1$ and for $\alpha > \alpha_U$. Simple poles due to zeros of γ^2 are present at $\alpha = \pm 1$. Also, depending upon the values of kb and of M, $\cosh kb\varpi$ may vanish along the real axis between α_L and α_U, thereby giving rise to $2N_p$ simple poles of $\mathcal{Y}$ in this region. The location of these poles to the left of $\bar{\alpha}$ are given by equation (82) for $\nu = n - (1/2),\ n = 1,\ 2,\ 3, \ldots,\ N_p$ with $\nu \leq kb/\pi\sqrt{1-M^2}$. The location of poles to the right, say $\alpha_\nu^{(+)}$, can be obtained from $\alpha_\nu^{(+)} = 2\bar{\alpha} - \alpha_\nu^{(-)}$. There also may be zeros located in the range $1 < \alpha < \alpha_U$. The locations of these zeros can generally be determined using a secant method; they alternate in order with poles that are present. We designate these roots as u_j with $j = 1,\ 2,\ 3, \ldots,\ N_z$. It is also easily deduced that the imaginary part of the kernel is identically zero in this range.

We know the path of integration lies above the singularities at -1 and $\alpha_\nu^{(-)}$, and below those at α, 1 and $\alpha_\nu^{(+)}$. To determine whether the N_z zeros lie in the upper or lower planes, we use equation (A.4) to determine the signs of the derivatives $\partial\alpha/\partial\delta$ for $\delta = 0$. In all cases studied thus far for both kernels Y and Z, this sign has been positive, indicating each zero belongs to the upper analytical region. Thus, we here assume the path of integration goes below these zeros.

As observed above, $\mathcal{Y}$ is real, positive, and regular outside the range $-1 < \alpha < \alpha_U$, and hence the (numerical) integrations in these regions is straightforward. However, within the range $-1 < \alpha < \alpha_U$, a suitable representation for $\ln \mathcal{Y}$ is required, and to aid us in this task it is useful to define a related function, say, ψ_S. This new function is defined such that $\arg(\mathcal{Y}e^{-i\psi_S})$ is continuous at the singular points of $\mathcal{Y}$. (Compare with Munt [16].) Here, the change in $\arg \mathcal{Y}$ as the point α moves from the left to the right of a singularity is always $\pm\pi$ since only simple zeros and poles are present. Whether the argument increases or decreases depends upon whether the singularity is a zero or a pole and whether the path goes above or below. Using our above knowledge of the singularities, we define ψ_S via the equation

$$\psi_S(\alpha) = \pi\{[H(\alpha-1) - H(\alpha+1)] + \sum_{n=1}^{N_p}[H(\alpha - \alpha_{n-(1/2)}^{(+)}) - H(\alpha - \alpha_{n-(1/2)}^{(-)})] - \sum_{j=1}^{N_z} H(\alpha - u_j)\}$$

or, more conveniently,

$$\psi_S(\alpha) = \pi \sum_{j=1}^{N_S} q_j\ H(\alpha - \lambda_j). \tag{B.7}$$

Here $H(x)$ is the unit step function, $N_S = 2N_p + N_z + 2$ the total number of singularities, q_j the coefficient (either ± 1) that corresponds to the jth singularity, and λ_j the location of the singularity.

We next define a function, say ψ_B, that takes into account changes in the branch of the logarithm function. This function has a form similar to that of ψ_S:

$$\psi_B(\alpha) = 2\pi \sum_{j=1}^{N_B} \tilde{q}_j \; H(\alpha - \tilde{\lambda}_j), \tag{B.8}$$

Here N_B is the number of such jumps and $\tilde{\lambda}_j$ the location of the jth jump. The coefficient $\tilde{q}_j$ is ± 1 and corresponds to whether the argument of $\mathcal{Y}$ is increasing (+) or decreasing (-) at $\tilde{\lambda}_j$. The locations of branch jumps $\alpha = \tilde{\lambda}_j$ are found by numerical solution of

$$\arg[\mathcal{Y}(\alpha)e^{i[\psi_a - \psi_S(\alpha) - \pi]}]_{\alpha=\tilde{\lambda}_j} = 0, \tag{B.9}$$

for $j = 1, 2, 3, \ldots, N_B$. Here, ψ_a, which we may restrict to the range $0 \leq \psi_a \leq \pi$, is a constant angle that may be used to adjust the location of branch jumps away from the λ_j singularities. Setting this quantity to π has been useful in the current investigation, but other values may be required for other Mach numbers and frequencies.

For α in the range $-1 < \alpha < \alpha_U$, we now write $\ln \mathcal{Y}$ as

$$\ln \mathcal{Y}(\alpha) = \{\ln_p[\mathcal{Y}(\alpha)e^{i[\psi_a - \psi_S(\alpha)]}] + i\psi_B(\alpha)\} + i[\psi_S(\alpha) - \psi_a], \tag{B.10}$$

where $\ln_p z$ denotes the principal branch of $\ln z$ with $-\pi < \arg z \leq \pi$. The imaginary part of the quantity in curly brackets is continuous in the given range of α, and the real part has only logarithmic singularities at the zeros and poles represented by the λ_j.

To proceed with the determination of $\mathcal{Y}_+(\alpha)$, we evaluate the half-residue term in equation (77) to obtain the expression

$$\ln \mathcal{Y}_+(\alpha) = \frac{1}{2} \ln \mathcal{Y}(\alpha) + \frac{1}{2\pi i} \mathcal{P} \int_{-\infty}^{\infty} \frac{\ln \mathcal{Y}(z) \; dz}{z - \alpha}, \tag{B.11}$$

where $\mathcal{P}$ denotes the principal value. Noting a key result of analytical integration,

$$\frac{1}{2\pi i} \mathcal{P} \int_{-1}^{\alpha_U} \frac{i\psi_S(z) \; dz}{z - \alpha} = \frac{1}{2} \left(\sum_{j=1}^{N_S} q_j \right) \ln_p(\alpha_U - \alpha) - \frac{1}{2} \sum_{j=1}^{N_S} q_j \ln_p |\lambda_j - \alpha|, \tag{B.12}$$

we find that $\mathcal{Y}_+(\alpha)$ can be efficiently calculated from the following equation for α in the range $-1 < \alpha < 1$:

$$\begin{aligned} \ln \mathcal{Y}_+(\alpha) = {} & \frac{1}{2}\{\ln_p[\mathcal{Y}(\alpha)e^{i[\psi_a - \psi_S(\alpha)]}] + i[\psi_B(\alpha) + \psi_S(\alpha) - \psi_a]\} + \\ & \frac{1}{2\pi i} \int_{-\infty}^{-1} \frac{\ln_p \mathcal{Y}(z) \; dz}{z - \alpha} + \frac{1}{2\pi i} \mathcal{P} \int_{-1}^{\alpha_U} \frac{\{\ln_p[\mathcal{Y}(z)e^{i[\psi_a - \psi_S(z)]}] + i\psi_B(z)\} \; dz}{z - \alpha} + \\ & \frac{1}{2} \left(\sum_{j=1}^{N_S} q_j \right) \ln_p(\alpha_U - \alpha) - \frac{1}{2} \sum_{j=1}^{N_S} q_j \ln_p |\lambda_j - \alpha| - \frac{\psi_a}{2\pi} \ln_p \left(\frac{\alpha_U - \alpha}{\alpha + 1} \right) \\ & + \frac{1}{2\pi i} \int_{\alpha_U}^{\infty} \frac{\ln_p \mathcal{Y}(z) \; dz}{z - \alpha}. \end{aligned} \tag{B.13}$$

The above equation is not valid for $\alpha = \lambda_j$, but any needed values of $\mathcal{Y}_+(\lambda_j)$ can be obtained by evaluating the above expression for nearby values of α and interpolating the results.

The principal value integral in the above expression is evaluated numerically as follows: Constants λ_j are placed in consecutive order to form subintervals, and integrations are performed over these individual ranges. A numerical method (e.g., the Gaussian-Kronrod adaptive method) that does not use endpoint evaluations is required. Only the integral over the range containing the point α needs to be calculated as a principal value.

The numerical integrations in the above formula can be time consuming, and so it is convenient to represent the functions $\tilde{Y}_+$ and $\tilde{Y}_-$ using splines, polynomials, or rational functions for real α within their respective domains, $\alpha \geq \bar{\alpha}$ and $\alpha \leq \bar{\alpha}$, of analyticity. Outside these respective domains but within the range $-1 < \alpha < 1$, the factors can be obtained from the relation $Y = \tilde{Y}_+\tilde{Y}_-$.

For our directivity calculation, we also need $\tilde{Y}_-(\alpha)$ and $\tilde{Z}_-(\alpha)$ for $\alpha = \alpha_\nu^{(-)}$ in the lower complex plane. These can be determined from equations of the type

$$\ln \mathcal{Y}_-(\alpha) = -\frac{1}{2\pi \mathrm{i}} \int_{-\infty+\mathrm{i}0}^{\infty-\mathrm{i}0} \frac{\ln \mathcal{Y}(z)\, dz}{z-\alpha}, \tag{B.14}$$

where the path of integration is the same as above except it is not deformed around α; i.e., there is no need to calculate the residue term or the principal value. Straightforward analysis shows that for α in the lower complex plane, $\mathcal{Y}_-(\alpha)$ may be calculated from

$$\begin{aligned}
\ln \mathcal{Y}_-(\alpha) = \\
&-\frac{1}{2\pi \mathrm{i}} \int_{-\infty}^{-1} \frac{\ln_p \mathcal{Y}(z)\, dz}{z-\alpha} - \frac{1}{2\pi \mathrm{i}} \int_{-1}^{\alpha_U} \frac{\{\ln_p[\mathcal{Y}(z)\mathrm{e}^{\mathrm{i}[\psi_a - \psi_S(z)]}] + \mathrm{i}\psi_B(z)\}\, dz}{z-\alpha} - \\
&\frac{1}{2} \sum_{j=1}^{N_S} q_j [\ln_p(\alpha_U - \alpha) - \ln_p(\lambda_j - \alpha)] + \frac{\psi_a}{2\pi} [\ln_p(\alpha_U - \alpha) - \ln_p(-1-\alpha)] - \\
&\frac{1}{2\pi \mathrm{i}} \int_{\alpha_U}^{\infty} \frac{\ln_p \mathcal{Y}(z)\, dz}{z-\alpha}.
\end{aligned} \tag{B.15}$$

As in the case for real α, the integral over the range $-1 \leq z \leq \alpha_U$ is to be subdivided into several integrals so that no pole or zero of the kernel is crossed during the course of evaluation.

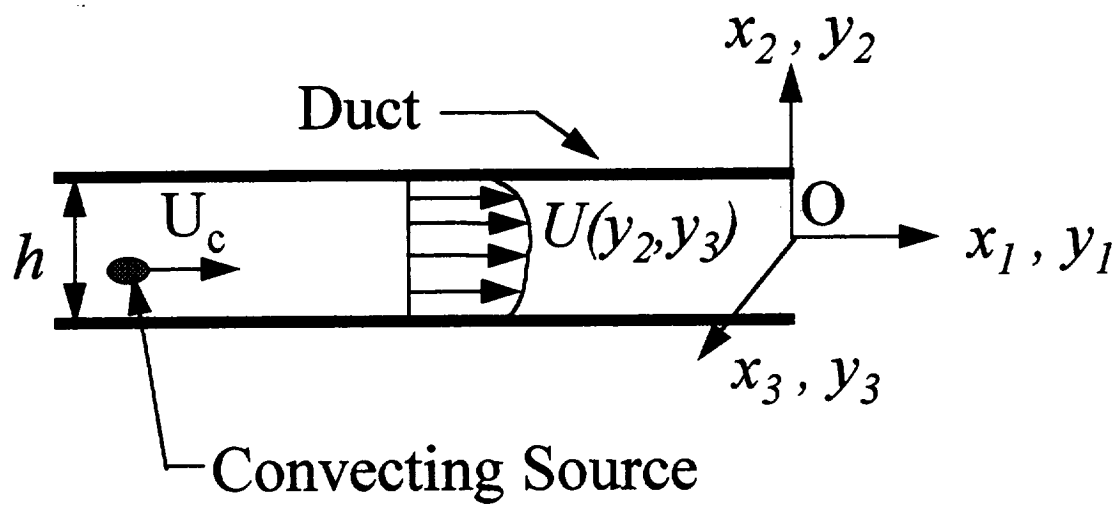

Fig. 1: Side view of jet with arbitrary mean velocity U. Convecting source displayed.

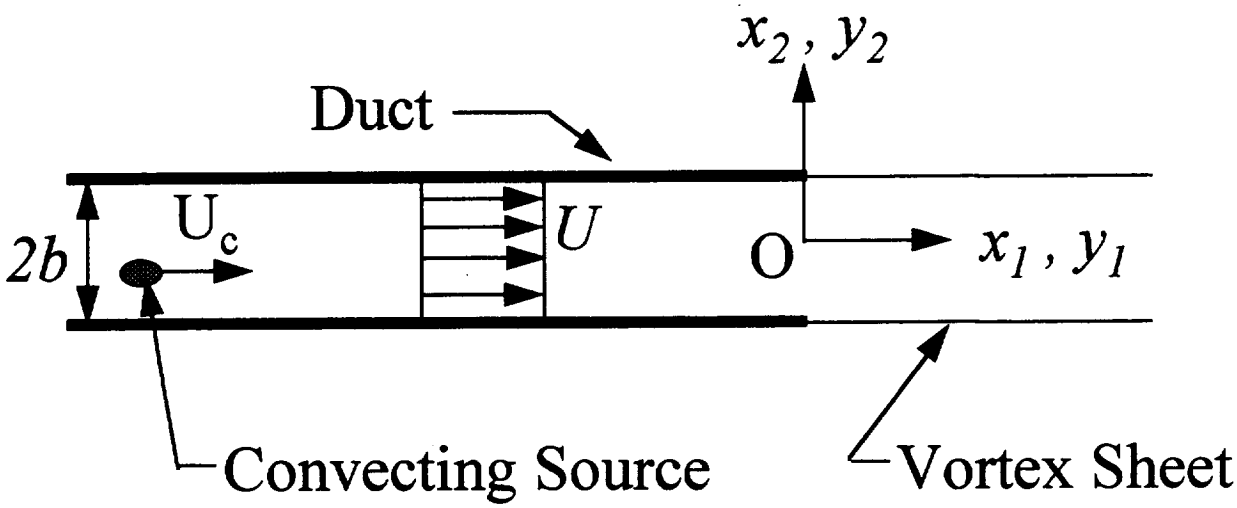

Fig. 2: Two-dimensional duct and plug-flow jet for Wiener-Hopf problem. Vortex sheet displayed.

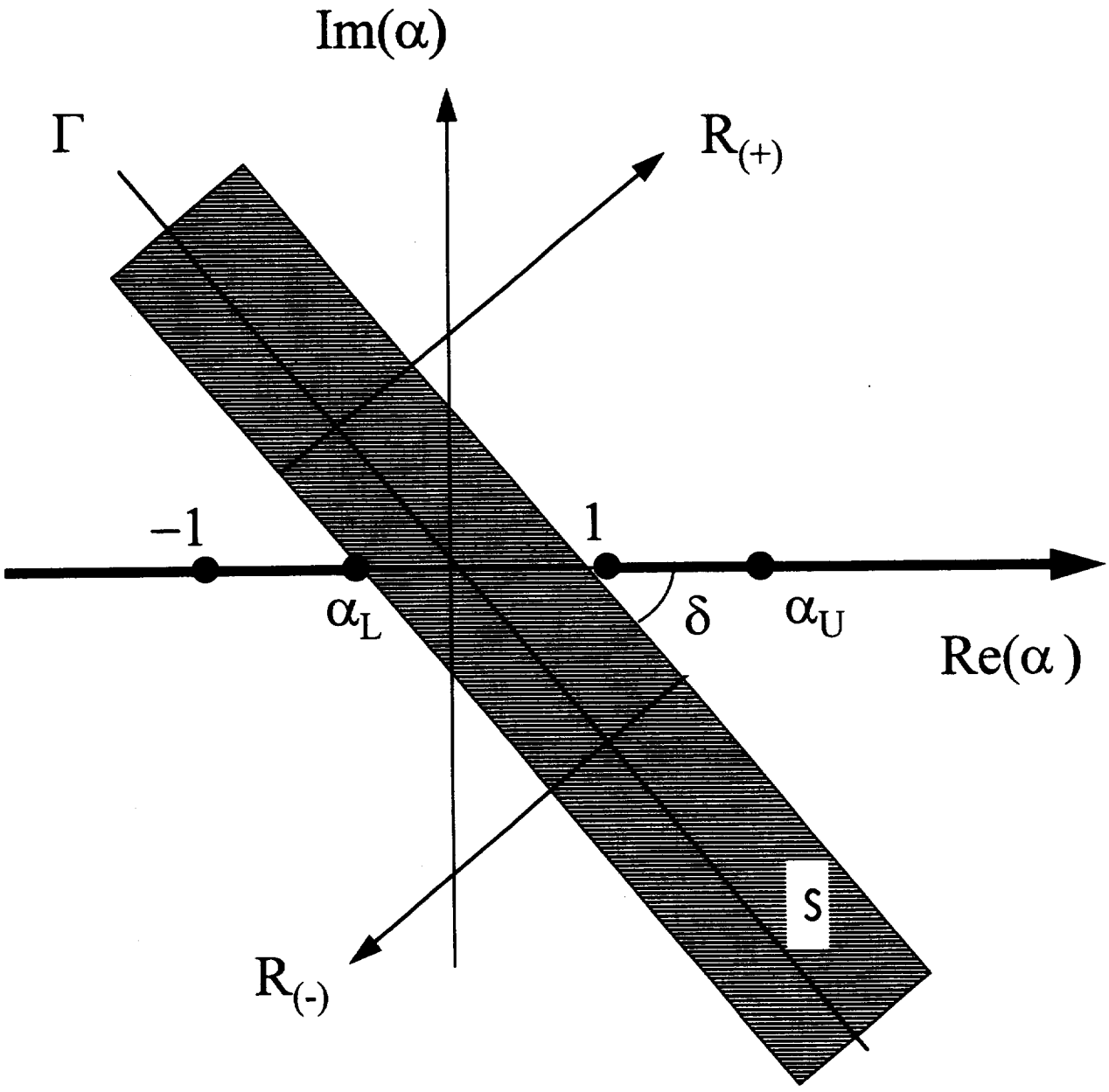

Fig. 3: The common strip S in the complex α–plane with plus and minus analytic regions indicated.

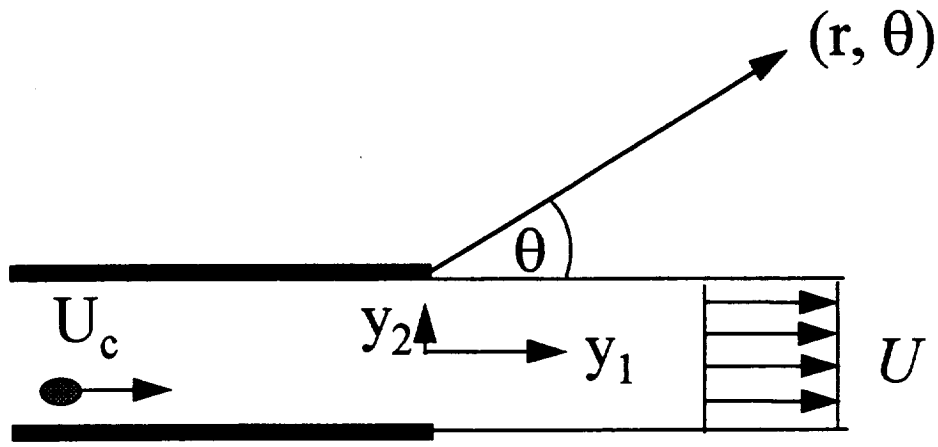

Fig. 4: Definition sketch of polar coordinates (r, θ). Also shows coordinates for moving eddy source at $\mathbf{y} = (y_1, y_2)$.

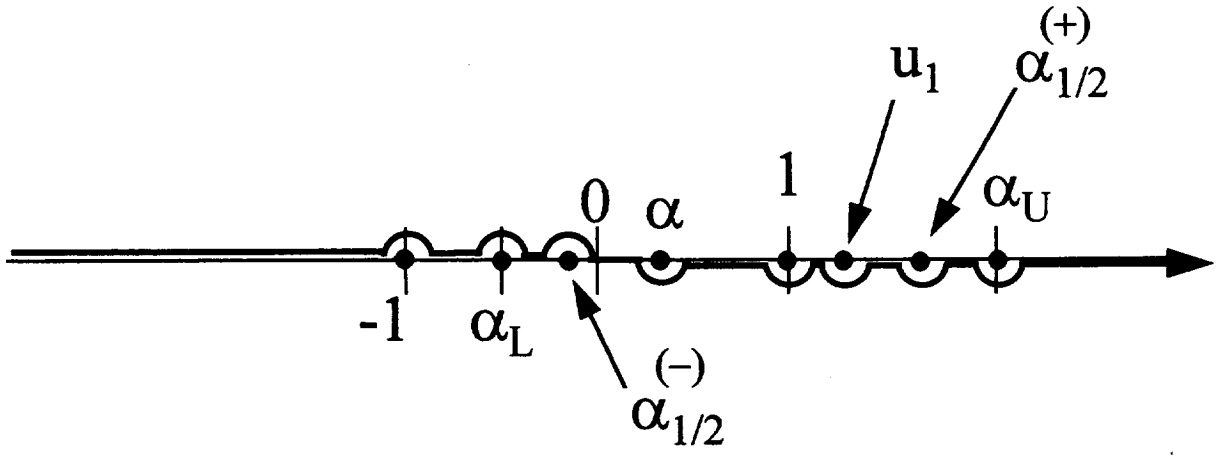

Fig. 5: Sketch of complex α-plane for factorization of Y showing contour of integration around singularities.

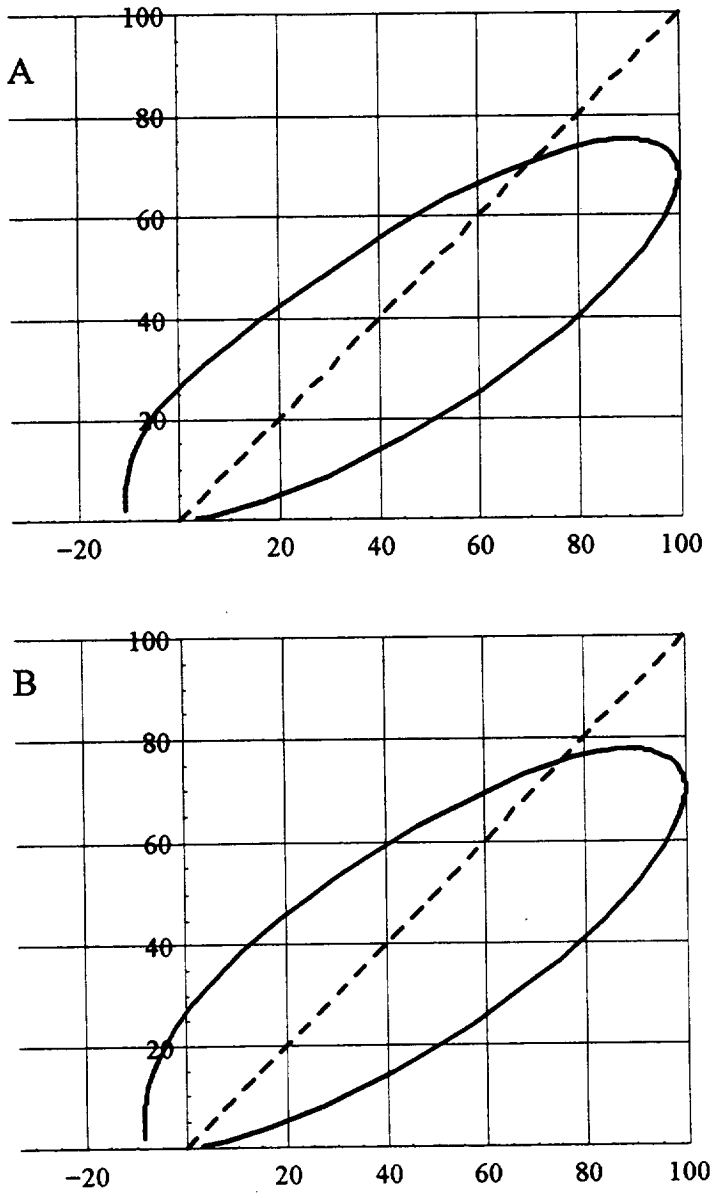

Fig. 6: Polar plot of scaled spectral density of the far-field intensity as a function of polar angle θ for frequency kb= 0.25 π, exit Mach number M= 0.3, convection Mach number M_c=0.15, y_1/b =-1.0, and (A) y_2/b=-0.875 and radius ratio b_0/b=0.25; (B) y_2/b=0 and b_0/b=0.25; (C) y_2/b=0.875 and b_0/b=0.25; and (D) y_2/b=0 and b_0/b=1. Dashed line shows region of instability wave. Q-values for the respective plots: 2.27 (10^{-3}), 2.18 (10^{-3}), 2.07 (10^{-3}), and 5.15 (10^{-3}).

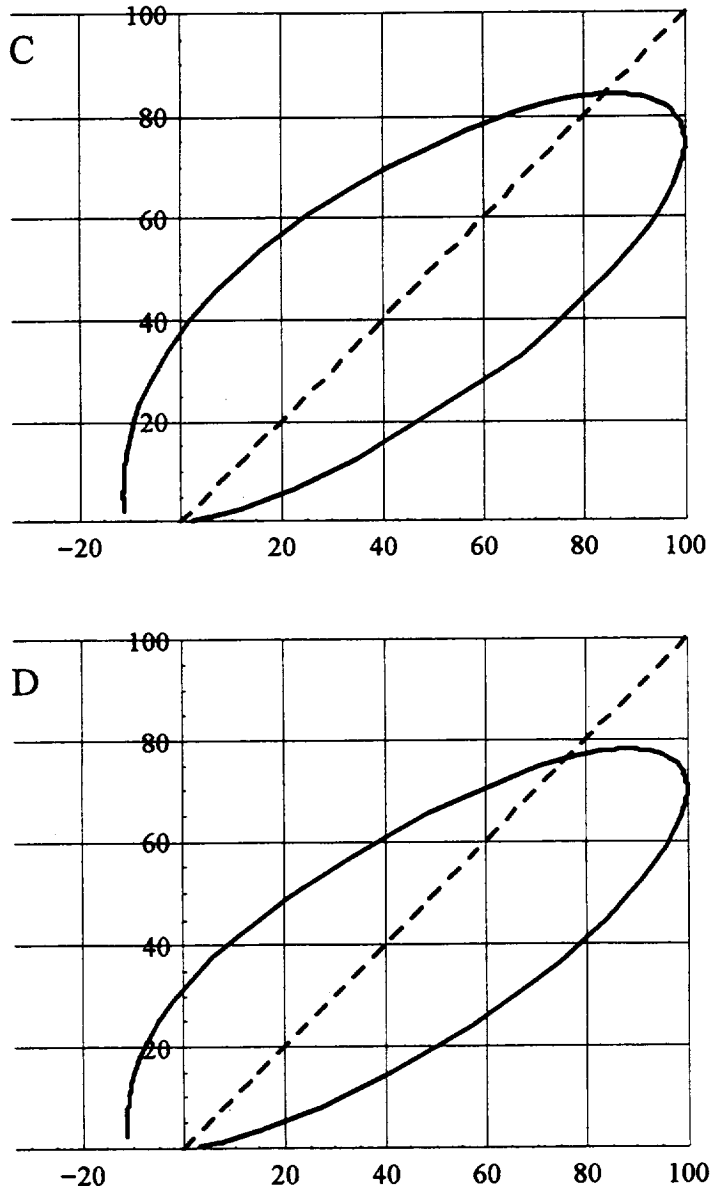

Fig. 6: Continued

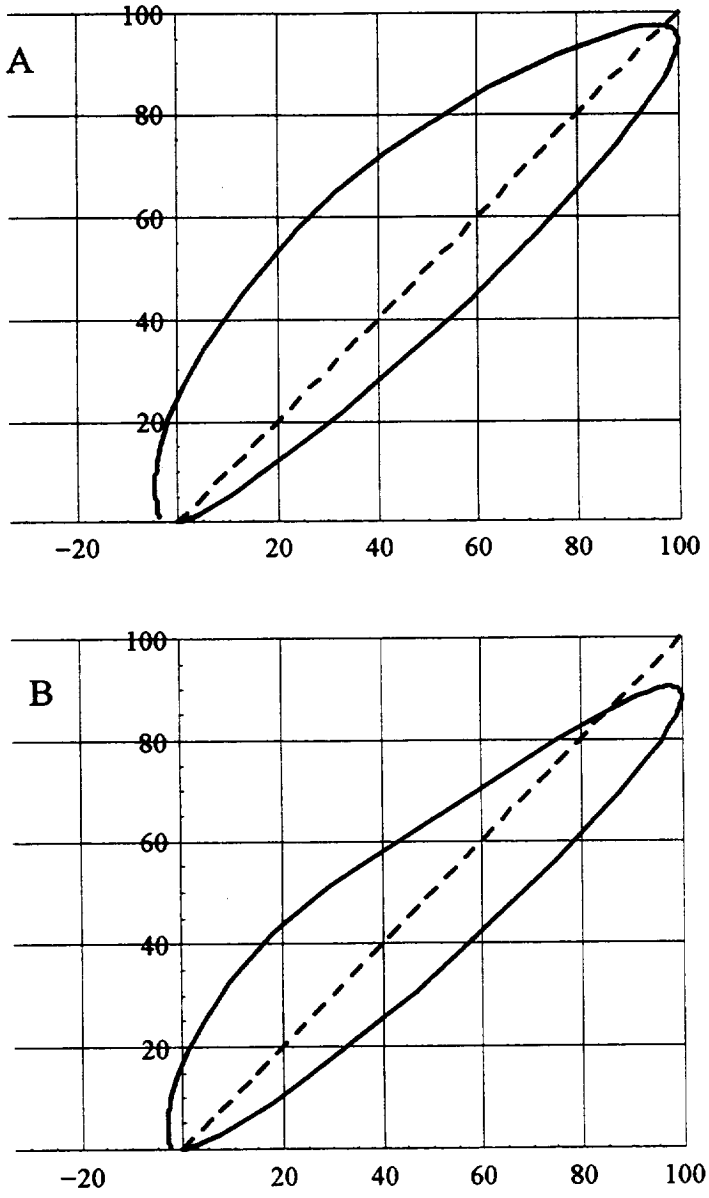

Fig. 7: Polar plot of scaled spectral density of the far-field intensity as a function of polar angle θ for frequency kb= 0.75 π, exit Mach number M= 0.3, convection Mach number M_c=0.15, y_1/b =-1.0, and (A) y_2/b=-0.875 and radius ratio b_0/b=0.25; (B) y_2/b=0 and b_0/b=0.25; (C) y_2/b=0.875 and b_0/b=0.25; and (D) y_2/b=0 and b_0/b=1. Dashed line shows region of instability wave. Q-values for the respective plots: 1.53 (10^{-3}), 1.34 (10^{-3}), 1.45 (10^{-3}), and 4.53 (10^{-3}).

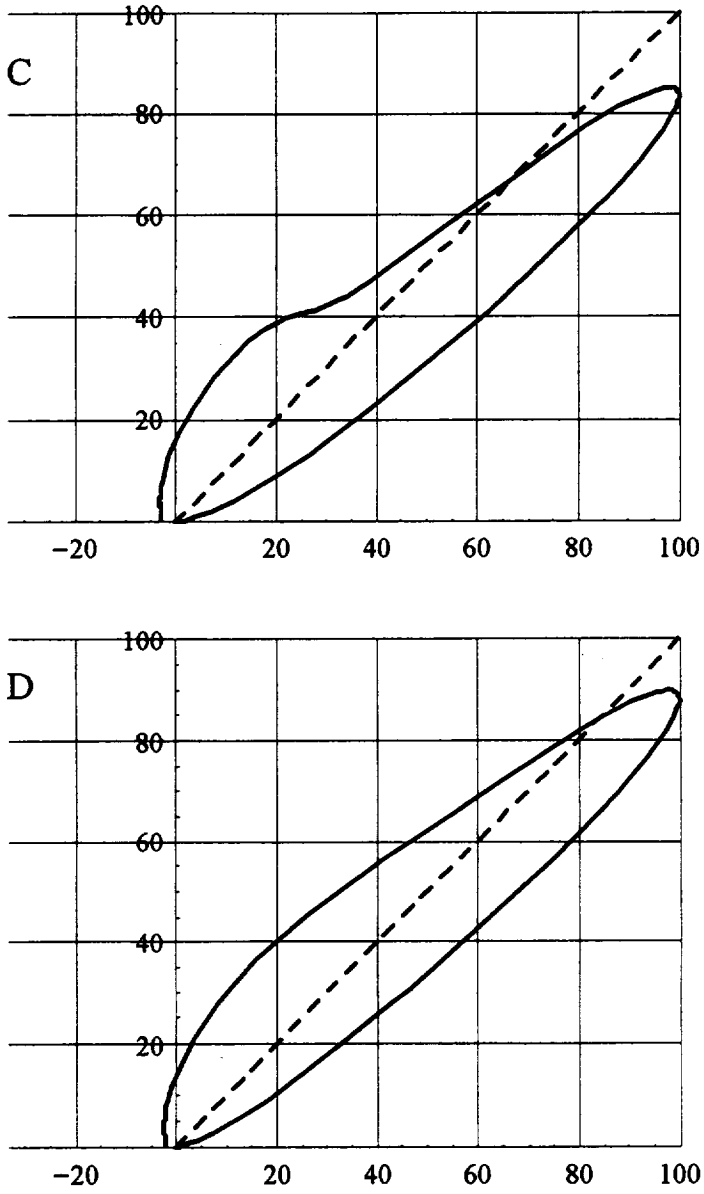

Fig. 7: Continued

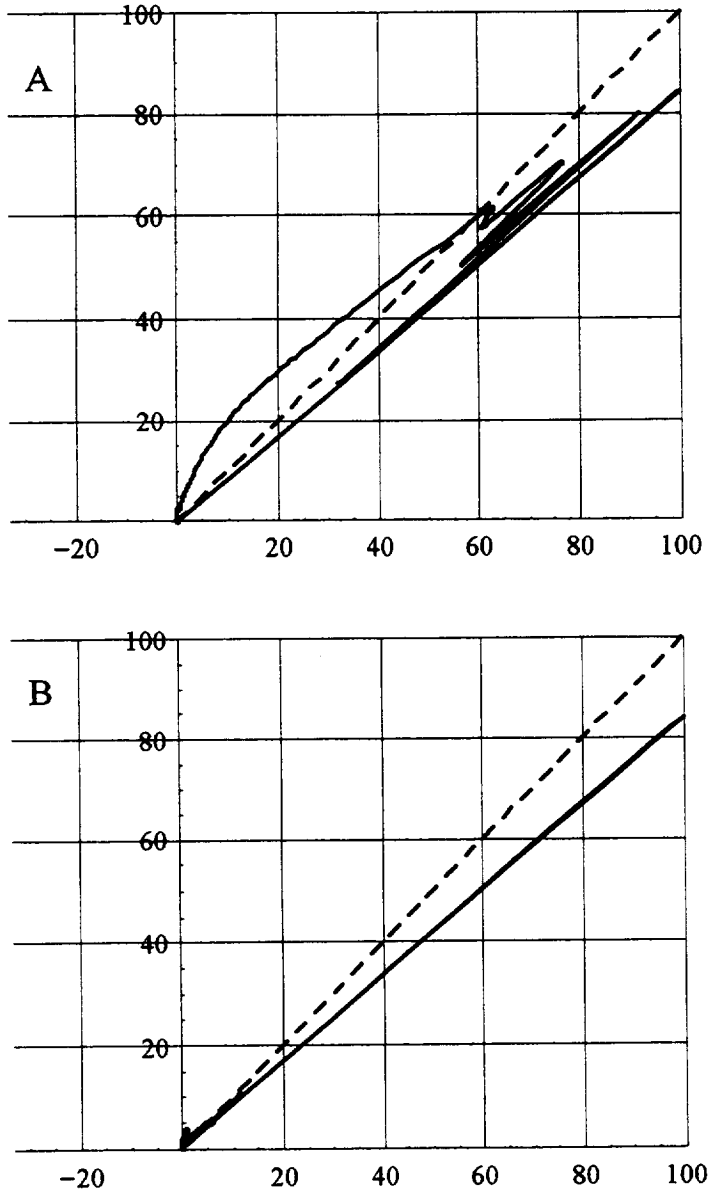

Fig. 8: Polar plot of scaled spectral density of the far-field intensity as a function of polar angle θ for frequency kb= 6π, exit Mach number M= 0.3, convection Mach number M_c=0.15, y_1/b =-1.0, and (A) y_2/b=-0.875 and radius ratio b_0/b=0.25; (B) y_2/b=0 and b_0/b=0.25; (C) y_2/b=0.875 and b_0/b=0.25; and (D) y_2/b=0 and b_0/b=1. Dashed line shows region of instability wave. Q-values for the respective plots: 2.55 (10^{-5}), 1.22 (10^{-4}), 2.81 (10^{-5}), and 5.21 (10^{-17}).

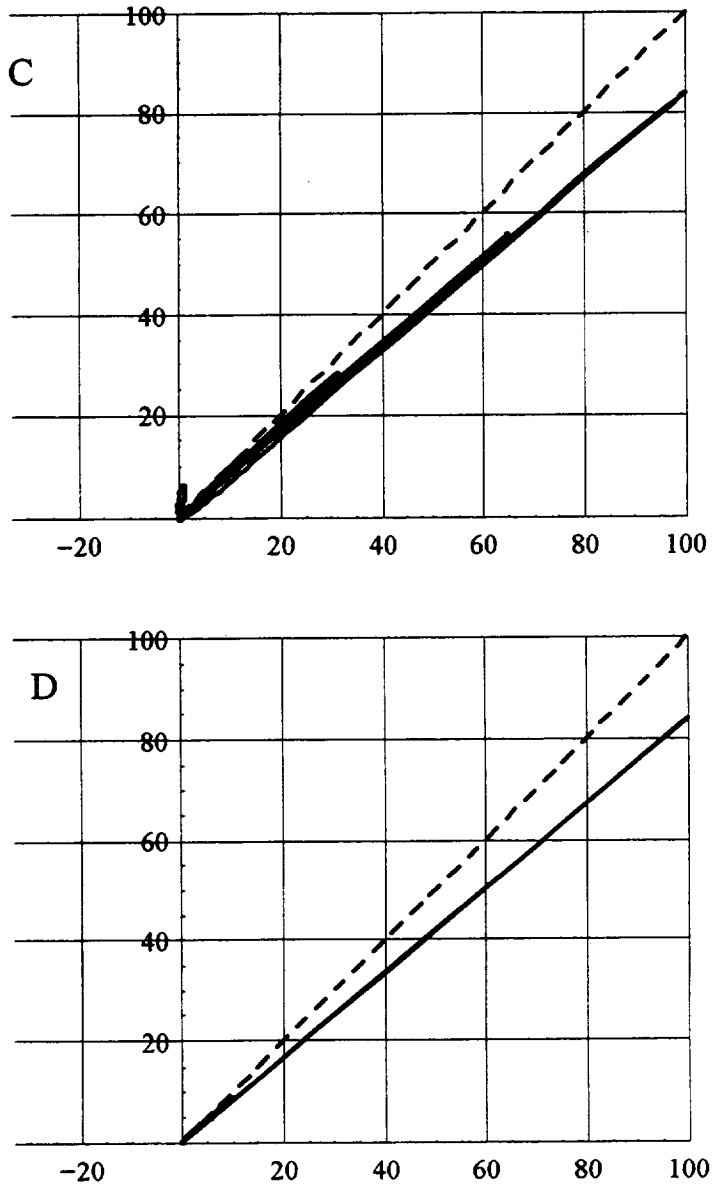

Fig. 8: Continued

REPORT DOCUMENTATION PAGE

Form Approved
OMB No. 0704-0188

1. AGENCY USE ONLY (*Leave blank*)	2. REPORT DATE	3. REPORT TYPE AND DATES COVERED
	May 1998	Technical Memorandum

4. TITLE AND SUBTITLE

Refraction of Sound Emitted Near Solid Boundaries From a Sheared Jet

5. FUNDING NUMBERS

WU-537-05-21-00

6. AUTHOR(S)

Loren H. Dill, Ayo A. Oyediran, and Eugene A. Krejsa

7. PERFORMING ORGANIZATION NAME(S) AND ADDRESS(ES)

National Aeronautics and Space Administration
Lewis Research Center
Cleveland, Ohio 44135-3191

8. PERFORMING ORGANIZATION REPORT NUMBER

E-11178

9. SPONSORING/MONITORING AGENCY NAME(S) AND ADDRESS(ES)

National Aeronautics and Space Administration
Washington, DC 20546-0001

10. SPONSORING/MONITORING AGENCY REPORT NUMBER

NASA TM—1998-207421

11. SUPPLEMENTARY NOTES

Loren H. Dill and Ayo A. Oyediran, AYT Corporation 2001 Aerospace Parkway, Brook Park, Ohio 44142, and Eugene A. Krejsa, NASA Lewis Research Center. Responsible person, Eugene A. Krejsa, organization code 5940, (216) 433-3951.

12a. DISTRIBUTION/AVAILABILITY STATEMENT

Unclassified - Unlimited
Subject Category: 71 Distribution: Nonstandard

This publication is available from the NASA Center for AeroSpace Information, (301) 621-0390.

12b. DISTRIBUTION CODE

13. ABSTRACT (*Maximum 200 words*)

A mathematical model is developed to describe the sound emitted from an arbitrary point within a turbulent flow near solid boundaries. A unidirectional, transversely sheared mean flow is assumed, and the cross-section of the cold jet is of arbitrary shape. The analysis begins with Lilley's formulation of aerodynamic noise and, depending upon the specific model of turbulence used, leads via Fourier analysis to an expression for the spectral density of the intensity of the far-field sound emitted from a unit volume of turbulence. The expressions require solution of a reduced Green's function of Lilley's equation as well as certain moving axis velocity correlations of the turbulence. Integration over the entire flow field is required in order to predict the sound emitted by the complete flow. Calculations are presented for sound emitted from a plugflow jet exiting a semi-infinite flat duct. Polar plots of the far-field directivity show the dependence upon frequency and source position within the duct. Certain model problems are suggested to investigate the effect of duct termination, duct geometry, and mean flow shear upon the far-field sound.

14. SUBJECT TERMS

Acoustics; Jet noise

15. NUMBER OF PAGES

51

16. PRICE CODE

A04

17. SECURITY CLASSIFICATION OF REPORT	18. SECURITY CLASSIFICATION OF THIS PAGE	19. SECURITY CLASSIFICATION OF ABSTRACT	20. LIMITATION OF ABSTRACT
Unclassified	Unclassified	Unclassified	